Doctoral Thesis

Study on Metal-Insulator Transition of $PrBaCo_2O_{5+x}$ using Diffraction and X-ray Spectroscopy

August, 2014

Ping Miao

Department of Materials Structure Science,

School of High Energy Accelerator Science

The Graduate University for Advanced Studies (SOKENDAI)

CONTENTS

Chapter 1 Introduction

Transition-metal oxides with perovskite structure present a wide variety of challenging phenomena. Superconductivity and colossal magnetoresistance (CMR) of Cu and Mn oxides are properties related with a complex strong correlation between charge, spin, orbital, and lattice degrees of freedom occurring in these materials. Cobalt oxides are also very good examples of how the strong correlation can influence the macroscopic properties. The competition between crystal field (CF), on-site Coulomb correlations, and the intra-atomic exchange energies leads to three possible spin states of Co^{3+} ions: the low spin state (LS, $t_{2g}^{6}e_{g}^{0}$), the intermediate spin state (IS, $t_{2g}^{5}e_{g}^{1}$), and the high spin state (HS, $t_{2g}^{4}e_{g}^{2}$). In many cobaltites the energy differences between spin states are small and can be easily overcome by thermal fluctuations, leading to spin state transitions. The fact that Co ions can easily present, in the perovskite structure, different spin states makes its strong correlation effect even more prominent than in other transition-metal oxides such as manganites or cuprates. Over the past 15 years, The A-site ordered perovskite-type cobaltites with the general formula $RBaCo_2O_{5+x}$ (R: lanthanoid elements or Y, $0 \leq x \leq 1$) have attracted considerable attention because of their unusual electric and magnetic properties such as metal insulator transition (MIT) and colossal magnetoresistance (CMR) [1–5]. The oxygen content x ($0<x<1$) controls the nominal valence of Co ions that varies from 3.5+ (50% of Co^{3+} and 50% of Co^{4+}) for x= 1 to 2.5+ (50% of Co^{3+} and 50% of Co^{2+}) for x = 0 passing through 100% of Co3+ for x = 0.5. The fundamental crystal structure of $RBaCo_2O_{5+x}$ is a "112" type layered perovskite structure composed of a stacking of [BaO] – [CoO_2] – [RO_x]– [CoO_2] along the c axis [Fig 1(a)] [1–5]. For stoichiometric $RBaCo_2O_{5.5}$, the oxygen vacancy ordering makes the alternative pyramidal and octahedral coordinations along b axis, thus resulting the "122" type $a_p \times 2a_p \times 2a_p$ (a_p is the parameter of pseudocubic perovskite subcell) unite cell doubling of lattice constant b [Fig 1(b)] [3–9].

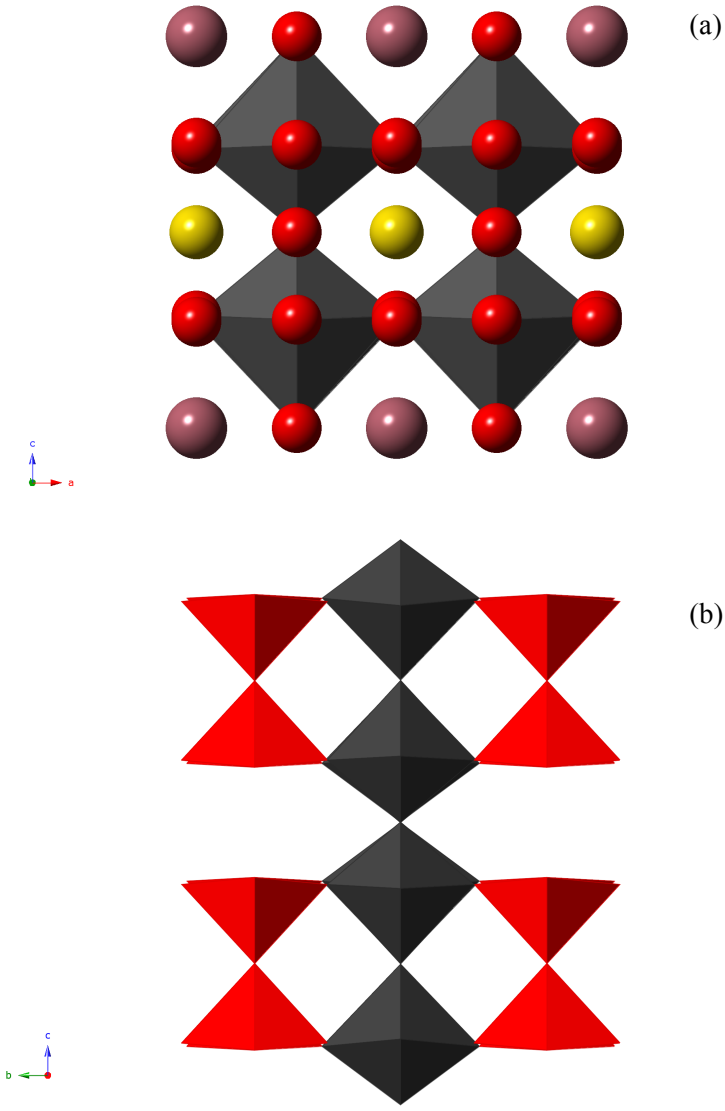

Fig. 1 (a) Cyrstal stucture of $RBaCo_2O_{5+x}$ (ac plane view), yellow sphere stands for Pr, purple for Ba, red for O, the black polyhedron for Co coordination. (b) Schematic drawing for oxygen ordering model of $RBaCo_2O_{5.5}$ (bc plane view), only Co-O polyhedrons are displayed.

Metal-Insulator Transition (MIT), , is a kind of phenomenon demonstrating huge resistivity changes, over tens of orders of magnitude, and has been widely observed in strongly correlated systems [10,11]. The terminology of "insulator" and "metal" is just to distinguish the large difference in resistivity, i.e, "metal" here is not necessarily to be a real metal, the resistivity of which decreases as the temperature goes down. In many systems with the property of MIT, even in the "metal" phase it can behave like a semiconductor. Much theoretical effort has been made to clarify the nature of this unconventional phenomenon since the early stage of condensed

matter physics, such as the Mott-Hubbard model, double exchange interaction etc. [12–18]. The MIT in $RBaCo_2O_{5+x}$ can be induced by temperature, pressure and hole doping as well [3,6,19–21]. Most of the effort has been focused on the temperature induced MIT of stoichiometric $RBaCo_2O_{5.5}$, which is accompanied by an anomaly in inverse magnetic susceptibility, as shown in Fig. 2 [6]. This anomaly is generally attributed to the spin state transition (SST) of Co^{3+} ions [6–9,22,23], while a minor regard it as charge ordering [24]. However, in the framework of SST, the spin states below and above the transition temperature are still in controversy. From magnetic measurements on several samples with different lanthanides, Maignan et al. first suggested a combination of IS pyramid (Co_{pyr}) and LS octahedra (Co_{oct}) for $T < T_{MI}$ [3]. Later, Moritomo et al. speculated that the MIT is induced by SST from an orbital-ordered (OO) IS state to the HS state in both Co_{pyr} and Co_{oct} sites, based on their crystal structure study on $TbBaCo_2O_{5.5}$ [6]. However, soon after that, a synchrotron radiation x-ray powder diffraction (XRPD) study by Frontera et al. on $GdBaCo_2O_{5.5}$ ruled out any orbital-ordering, suggesting that the MIT should be related to a spin-state switch from LS to HS states at Co_{oct} while the Co_{pyr} should remain in IS state at both sides of the MIT [9]. Taskin et al. proposed a combination of IS pyramid (Co_{pyr}) and LS octahedra (Co_{oct})for $T < T_{MI}$ by extrapolating the saturated magnetic moment at T = 0 K in single crystal $GdBaCo_2O_{5.5}$ [22]. The NMR studies carried out on a single-crystal sample by Soda et al. suggested IS or HS states at Co_{pyr} while LS at Co_{oct} at insulating phase [23].

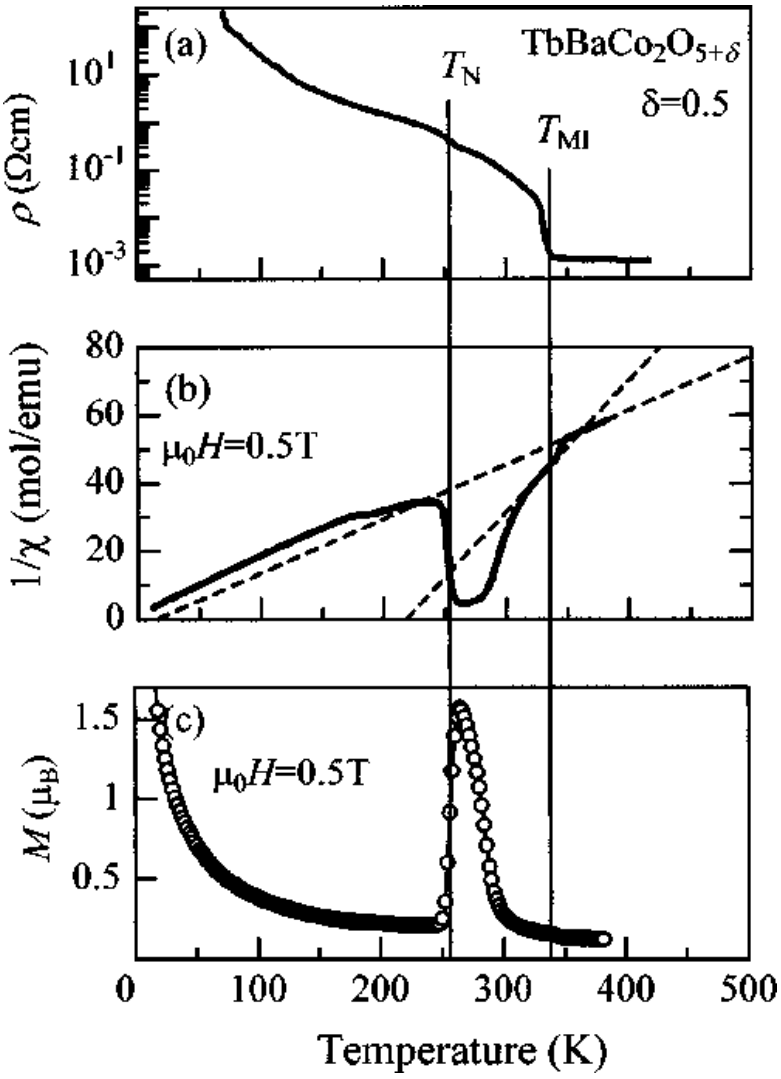

Fig. 2 Temperature dependence of (a) resistivity ρ, (b) inversesusceptibility 1/χ, and (c) magnetization M of polycrystalline $TbBaCo_2O_{5.5}$. M were measured under a field of 0.5 T after cooling down to 5 K in the zero field (ZFC). T_{MI} and T_N represent critical temperatures for the metal-insulator transition and Neel temperature, respectively. Broken lines in (b) are the Curie-Weiss fittings [6].

Neutron magnetic diffraction is an effective probe to detect the spin state. There are several magnetic phases in $RBaCo_2O_{5.5}$ with dependence on the temperature [25–27]. As MIT temperature T_{MI} is generally higher (or equal to) the first magnetic transition (from paramagnetic phase to magnetic ordering phase) temperature T_c, the magnetic phase just below T_c is believed to be mostly related to the MIT phase transition. To establish the correct magnetic model, it is essential first to clarify the real crystal structure. At preliminary stage, people believed an isomorphic crystal structure phase transition occurring together with the MIT

transition, where the orthorhombic Pmmm ($a_p \times 2a_p \times 2a_p$) crystal structure keeps unchanged under the transition [6–9]. As a result, several neutron magnetic diffraction studies were just based on the crystal structure with space group of Pmmm in $a_p \times 2a_p \times 2a_p$ (or even $a_p \times a_p \times 2a_p$) unite cell [28–30]. However, Chernenkov et al. first found superlattice peaks in the insulating phase and disappearing in the metal phase in $GdBaCo_2O_{5.5}$ by single crystal x-ray diffraction, and thus concluded that the structural phase transition coupling with MIT is from orthorhombic Pmmm ($a_p \times 2a_p \times 2a_p$) to orthorhombic Pmma ($2a_p \times 2a_p \times 2a_p$) [31]. This phenomenon was later oberserved in $RBaCo_2O_{5.5}$ with other rare earth elements such as, Dy, Tb, Nd by single crystal x-ray diffraction as well [32,33]. In the case of Ho and Y, a monoclinic P112/m ($2a_p \times 2a_p \times 2a_p$) were found to be the real structure for insulating phase while the metal phase remains Pmmm ($a_p \times 2a_p \times 2a_p$) [24,34,35]. Actually, it may be necessary to separate Ho and Y from other rare earth element Ln (Ln: from Pr to Dy), because T_{MI} seems to coincide with T_c for Ho and Y, while T_{MI} is higher than T_c for Ln.

Plakhty et al. established a ferrimagnetic ordering model based on the Pmma ($2a_p \times 2a_p \times 2a_p$) crystal structure for magnetic ordering phase just below T_c by neutron powder diffraction study on $TbBaCo_2O_{5.5}$ [26]. The Pmma ($2a_p \times 2a_p \times 2a_p$) crystal structure consisted two nonequivalent pyramidal Co sites and two nonequivalent octahedral Co sites. By Rietveld refinement, Plakhty et al. concluded that one of the pyramidal Co^{3+} site is HS state while the other sites cannot be clearly assigned. The magnetic model and crystal model arise from the symmetry analysis although no super lattice peak from Pmma ($2a_p \times 2a_p \times 2a_p$) was observed in the diffraction pattern [26]. Even an effort by neutron single crystal diffraction failed in finding any super lattice peak [23]. So far, no evidence from neutron diffraction has been reported. This magnetic model was later supported by a muon spin relaxation measurement [27].

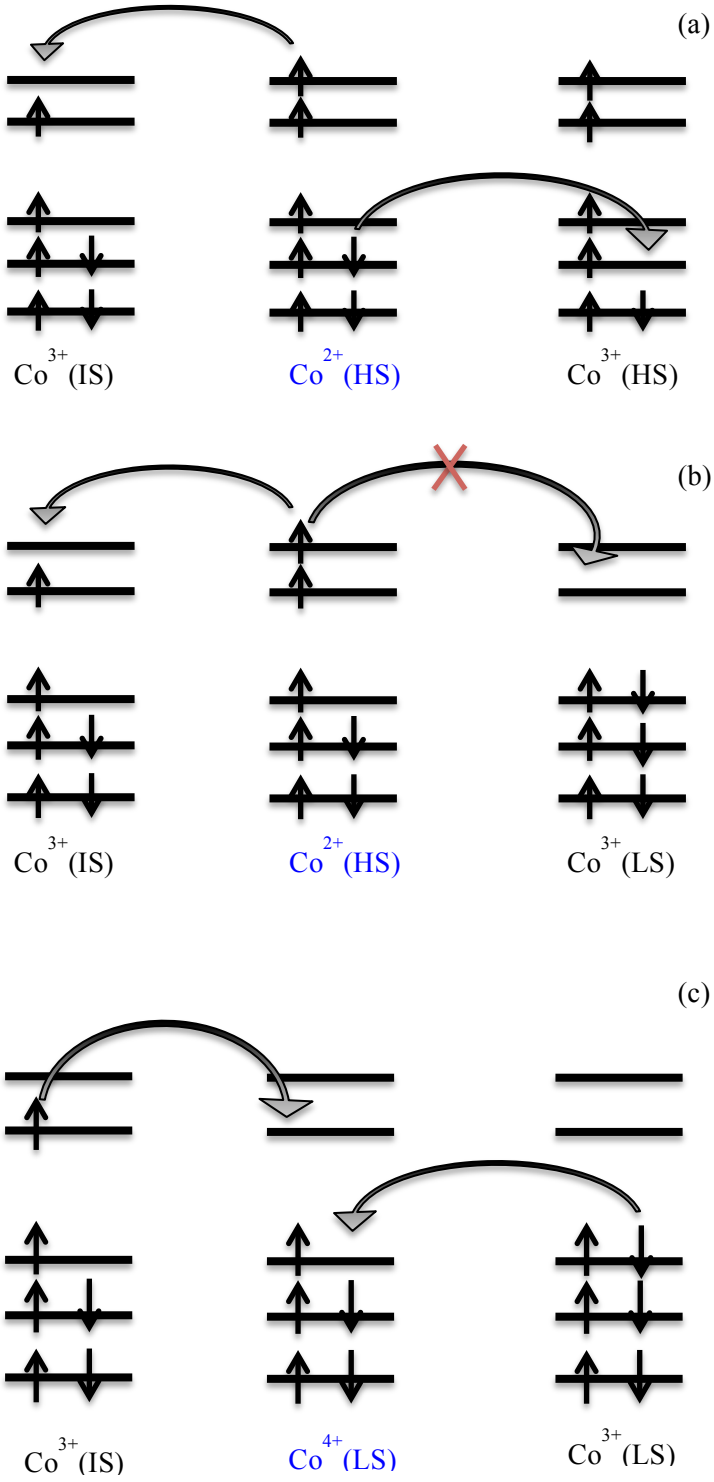

Fig. 3 The scheme showing the processes of electron (Co^{2+}) in (a),(b) and hole (Co^{4+}) in (c) hopping on the background of the HS and IS Co^{3+} (a) and LS Co^{3+} (b),(c). (a) applies to the high temperature metallic phase of $HoBaCo_2O_{5.5}$, whereas(b),(c) correspondsto the processes available at the low temperature insulating phase of $HoBaCo_2O_{5.5}$, illustrating the phenomenon of the spin blockade for electron hopping. Reproduced from Ref. [36] .

Based on the spin state transition (SST), Maignan et al. proposed a so called "spin blockade" mechanism for the temperature induced MIT of $RBaCo_2O_{5.5}$, assuming that IS pyramidal Co^{3+} ions and HS octahedral Co^{3+} ions consist in high temperature metal phase and the octahedral Co^{3+} ions switch to LS state in low temperature insulating phase [36]. This mechanism attribute the conductivity to the electrons of Co^{2+} ions and holes of Co^{4+} ions, arising from the thermal excitation of Co^{3+} since the nominal valence of $RBaCo_2O_{5.5}$ is 3+. The Co^{2+} ions are always in a HS state owing to a weaker crystal field than for Co^{3+} ions, and Co^{4+} ions are always in a LS state owing to a stronger crystal field. The main idea is that the mobility depends strongly on the spin state of the background Co^{3+}. Indeed, when one considers the motion of an extra electron on a background of a lattice of HS or IS Co^{3+} ions [Fig. 3(a)], it can be seen that one can easily move an extra electron from the middle HS Co^{2+} ion in both to the HS and IS Co^{2+} (to the left and to the right), i.e., one can interchange corresponding ionic states by moving one electron. The situation is, however, quite different if the background Co^{3+} are in a LS state [Fig. 3(b)] at low temperature phase. If one of the electrons of Co^{2+} is moved to the neighboring Co^{3+} ion, both ions will end up in a wrong spin state: Co^{2+} created at the right side in Fig. 3(b) will be in a LS state, and Co^{3+} left behind [middle in Fig. 3(b)] will be in the IS state. Thus, this electron hopping from HS Co^{2+} ion to LS Co^{3+} ion will be strongly suppressed, which is called a "spin blockade". However, also in the low temperature insulator phase with LS Co^{3+} background, the hole of LS Co^{4+} ion can easily move without any spin blockade, as shown in Fig. 3(c). Maignan et al. argues that this hopping of t_{2g} electron remains small in comparison to the Co^{2+} electron predominantly moving in a broad e_g band, for the explanation of the high resistivity in low temperature insulator phase.

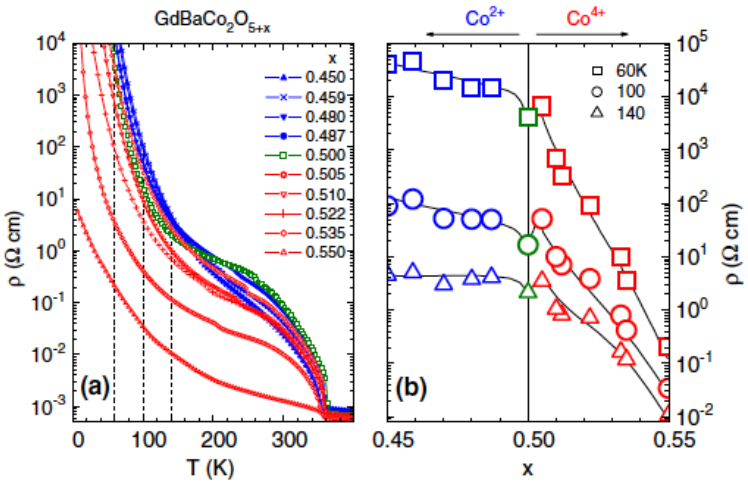

Fig. 4 (a) Temperature dependences of the inplane resistivity ρ(T) of $GdBaCo_2O_{5+x}$ crystals with oxygen content close to x = 0.5. (b) Doping dependences of the in-plane resistivity ρ(x) of $GdBaCo_2O_{5+x}$ crystals at several temperatures [20].

Later, Taskin et al. also take "spin blockade" model into account as the reason for the electron-hole asymmetry they found in $RBaCo_2O_{5+x}$, as shown in Fig. 4 [20]. This electron-hole asymmetry indicates the hole doping induced MIT of $RBaCo_2O_{5+x}$ if we increased the doping to higher level as will be demonstrated in our study below. Taskin et al. adopted the same spin state configuration for Co^{3+} ions as Maignan et al. do, that is half of them are in LS state and rest are in IS state. They assume that throughout the doping range, the spin state of Co^{3+} ions maintains not to be changed. Electron doping creates the HS Co^{2+} ion, whose e_g electron is hard to hop towards the neighboring LS Co^{3+} ion because "spin blockade" mechanism as shown is shown in Fig. 3(b). On the other hand, t_{2g} electron of LS Co^{3+} ions can easily move to the LS Co^{4+} ions created by hole doping by just interchange the atomic position, which is account for the high conductivity for the hole doping sample. This is actually contrary to Maignan et al.'s arguments, which assumes a low mobility for t_{2g} electrons. In a word, the "spin blockade" model cannot simultaneously explain the MITs induced by both temperature and hole doping.

Chernyshov et al. later discovered the pressure induced MIT in $TbBaCo_2O_{5.5}$. They suggested the structural phase transition to be from orthorhombic Pmmm ($a_p \times 2a_p \times 2a_p$) to orthorhombic Pmma ($2a_p \times 2a_p \times 2a_p$), same as that of temperature induced MIT, by the similarity of the lattice constant evolution in both cases [21]. For the hole doping induced MIT, the diffraction studies

suggested a tetragonal P4/mmm ($a_p \times a_p \times 2a_p$) crystal structure for $x > 0.6$ [19,37,38]. On the basis of the tetragonal crystal structure, Frontera et al. built the canted G-type antiferromagnetic structure for $PrBaCo_2O_{5.75}$ [37]. It should be noted that quite little attention was paid to the pressure and hole doping induced MITs.

This short and not comprehensive review of the past work on $RBaCo_2O_{5+x}$ (R: lanthanoid elements or Y, $0 \leq x \leq 1$) demonstrates that many unknown issues still exist, especially the mechanisms for MITs induced by temperature, pressure and oxygen content, which is motivation for us to further study MITs of $RBaCo_2O_{5+x}$.

Chapter 2 Synthesis

2.1. Synthesis Procedure

$LnBaCo_2O_{5+x}$ (Ln: Pr & Nd) composite oxides can be synthesized using the simple solid state reaction method [39,40]. We adopted a combined EDTA–citrate complexing sol–gel process for the sake the high crystallinity and time efficiency [41,42]. $Ba(NO_3)_2$, $Co(NO_3)_2$•xH2O and $Pr(NO_3)_2$•xH2O (or $Nd(NO_3)_2$•xH2O) served as the raw materials for the necessary metal ions. Separate 0.5 mol/L solutions of the nitrates were prepared by dissolving into deionized water, and their precise concentrations were determined by titration with EDTA (Concentrations of EDTA was determined by ZnCl solution). From these solutions, mixture was prepared with molar ratios of total metal ions:citric acid of 1:1:2. The mixed solution was then heated continuously at 90 °C for evaporating the water to get the gel. Then the gel was pre-fired in an intermediate temperature electrical box furnace at 120 °C for 3 h, 150 °C for 5 h, 180 and 210 °C for 6h to get the precursor, and at 300 °C for 3 h and 500 °C for 12h to remove the organic residues. The obtain powder was sintered in a high temperature electrical box furnace at 1200 °C for 24 h following by annealing at 1100 °C for 24 h, and waited for naturally cooling down. In this way, we can get the as-synthesized sample.

2.2. Crystallinity Enhancement

The as-synthesized sample was initially obtained without annealing at 1100 °C, and it was found by XRD characterization that some second phase existed in some of the copies, as shown by the impurity peak at about 31° of 2θ, close to the strongest peak in Fig. 5 (a). Searching in Inorganic Crystal Structure Database (ICSD), we couldn't specify the exact structure for this second phase. At first, we doubted that the impurity was due to the imperfect ratio of metal ions in the reactant, in other words, it is very sensitive to the ideal ratio, 1:1:2 for the Ln, Ba, Co ions. So the trial synthesis with various ratios, listed in Table 1, was performed and the resulted samples were characterized by XRD measurement [Part of the patterns is shown in Fig. 5 (b)]. It is exhibits that the even with a deviated proportion (Copy 18), it is also possible to get the pure phase, which means that the impurity does not come from the preparation of the mixed solutions. By taking into account the fact that the impurity occurs randomly in the as-synthesized samples, we tried to increase the sintering temperature and after that add a process of annealing at 1100 °C. It is found that not just impurity was significantly eliminated, but also the crystallinity was much improved, as shown in terms of the full width at half maximum (FWHM) of Bragg peaks in Table 2.

Table 1. Ratio of the metal ions in the mixed solutions for each synthesis.

Copy number	Co	Ba	Nd
13	2	1	1.05
14	2	1	1
15	2	1	0.95
16	2	0.95	1.05
17	2	0.95	1
18	2	0.95	0.95
19	2	0.91	1
20	2	1	0.85
21	1.89	1	1
22	2	0.91	0.91
23	1.89	0.91	1
24	1.89	1	0.91

Some unexpected problem appears when we tried to improve the efficiency by some changes in the synthesis procedure. Initially, the mixture of solutions was dried in an evaporating dish on the electric stove, where it was only one dish at one time, at 90 °C for evaporating the water to get the gel. The change we later made is that the intelligent multi-point magnetic stirrer (with heater) was adopted to dry several beakers of mixtures simultaneously for the first step and then put them into a baking oven to totally dry them and get the gel. Such a small change caused the random impurities same as shown in Fig. 5 (a) in the samples, for example, 10 copies were synthesized at one time and 4 of them had impurities by XRD characterization. So the problem is highly associated with the process on the stirrer. Then we tried to alter some parameters of the stirrer by lowering the speed of stirring, the heating temperature to prevent the spilling of the solution and shorting the time on the stirrer in case of inhomogeneous mixing of the reactants. However, the existence of some impure sample is inevitable although the time to synthesize one batch of samples is much shorter in this way. A large amount of samples had been synthesized after all these tests, so we started to think of ways to removed the impurities from the as-synthesized samples. It is founded that by re-sintering the sample most of impurities can be eliminated, with oxygen content variation x to be about 0.70. Since the samples were well divided by beakers outside and later small crucibles in the furnace, the pure ones were selected by XRD characterization for the further oxygen content control.

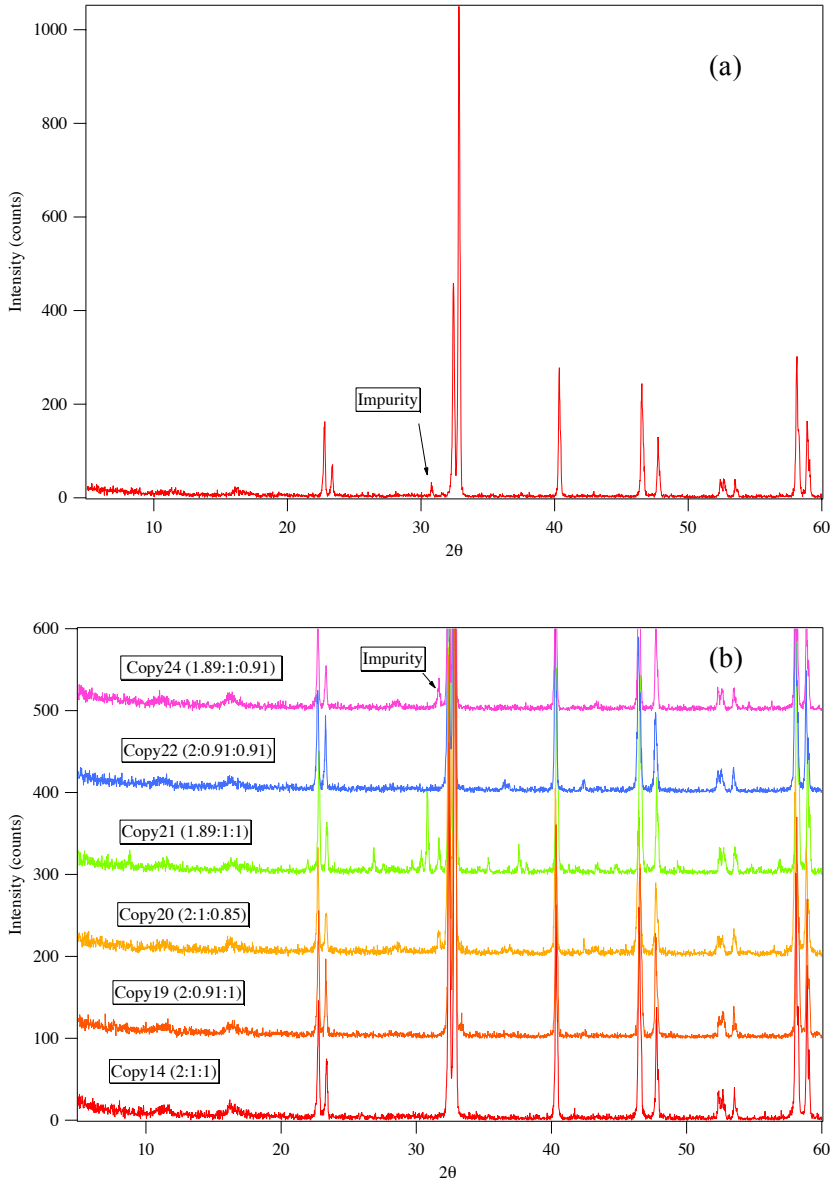

Fig. 5 (a) XRD pattern of the as-synthesized sample without annealing at 1100 °C (b) XRD patterns of samples with the various ratios of metal ions in the reactants.

Table 2. Peaks width from XRD at different synthesis conditions: Reaction at 1150° for 25 h; Reaction at 1200° for 24 hours and annealed 1100° at for 24 h; Reaction 1150° at for 24 h and annealed at 1100° for 24 h, respectively.

1150° & none		1200° & 1100°		1150° & 1100°	
2θ(°)	FWHM(°)	2θ(°)	FWHM(°)	2θ(°)	FWHM(°)
22.78	0.165	22.7	0.141	22.74	0.141
23.32	0.141	23.26	0.141	23.28	0.141

32.44	0.165	32.34	0.141	32.38	0.141
32.82	0.165	32.74	0.141	32.78	0.141
40.32	0.165	40.24	0.141	40.26	0.141
46.52	0.165	46.42	0.165	46.44	0.165
47.64	0.165	47.6	0.165	47.62	0.165
52.4	0.165	52.3	0.141	52.32	0.141
52.66	0.165	52.56	0.141	52.58	0.165
53.44	0.165	53.38	0.165	53.4	0.141
58.08	0.165	57.98	0.165	58	0.188
58.82	0.165	58.76	0.141	58.78	0.165

2.3. Oxygen Content Control

2.3.1 Iodometric Titration

The oxygen content of the as-synthesized sample was determined by iodometric titration method. The principle of iodometric titration is that by dissolving the $LnBaCo_2O_{5+x}$. sample in dilute hydrochloric acid (HCl) containing potassium iodide (KI), a reduction–oxidation reaction would take place, where Co^{4+} or Co^{3+} cations are reduced to Co^{2+} while iodide ions are oxidized to iodine. Thus, the oxygen content can be calculated from the amount of iodine obtained, which is in turn determined by titration with sodium thiosulfate ($Na_2S_2O_3$).

A typical procedure is as following: the sample (0.1~0.15 g, with 0.0001 g accuracy) was immersed in 10 ml de-ionized water in an Erlenmeyer flask, and an excess amount of KI (~2 g) was added to the mixture; after totally dissolving the KI, 5 ml of 6 mol L−1 HCl was added; the flask was slightly shaken and kept in the dark for 1 min to enable the sample to be dissolved. Then 50mL of water was added to the solution before titrated by $Na_2S_2O_3$ solution (0.05 mol/L, calibrated by $K_2Cr_2O_7$ standard solution). During the titration, the dark yellow color of the solution underwent a gradually lightening process, and 2–3 drops of 0.5% starch indicator were added when starting to fade away so that the color became dark again. The end point was reached when the color changed from dark blue to light pink. The oxygen content variation x was calculated by the following equation:

$$x = \frac{V_{Na_2S_2O_2} c_{Na_2S_2O_2} (A_{Pr}+A_{Ba}+2A_{Co}+5A_O)\text{-}m}{2m\text{-}16V_{Na_2S_2O_2} c_{Na_2S_2O_2}} \quad (1)$$

Here, m is the weight of sample, A_{Pr}, A_{Ba}, A_{Co} and A_O are the atomic weight of Pr, Ba, Co, and O respectively, $V_{Na_2S_2O_2}$ stands for the volume of $Na_2S_2O_3$ consumed and $c_{Na_2S_2O_2}$ the concentration of it. The titration was performed for several times to ensure the precision. Using this method, the oxygen content variation x of the as-synthesized $PrBaCo_2O_{5+x}$ was determined to be about 0.74 and that of $NdBaCo_2O_{5+x}$ is about 0.69.

2.3.2 Synthesis of Powder-Form Stoichiometric $PrBaCo_2O_{5.5}$

Since as-synthesized $PrBaCo_2O_{5.74}$ possesses the highest oxygen content in the system $RBaCo_2O_{5+x}$ (R: lanthanoid elements or Y, $0 \leq x \leq 1$), [42] it was adopted for obtaining the $PrBaCo_2O_{5+x}$ with a large range of oxygen concentrations by oxygen reduction, particularly for the stoichiometric $PrBaCo_2O_{5.5.}$ The reduction was performed by annealing the as-synthesized sample in a tubular furnace of pure nitrogen atmosphere at various temperatures for tens of hours and waited for naturally cooling after that. To ensure the homogeneity, the as-synthesized bulks were ground into powder before annealing.

The titrated oxygen contents for different conditions are in Table 3. We first chose to anneal at 900 ℃ in pure nitrogen atmosphere to see the limit for reduction of the oxygen. After several trial experiments, we finally found that the oxygen content variation x at thermodynamic equilibrium in this condition is around 0.18. Then these samples of low oxygen content were put back to the high temperature furnace and annealed again at 1100 ℃. The resultant oxygen content variation x returned to 0.70, exhibiting a good reversibility, which would be very convenient for us to do trial experiments of oxygen reduction as it requires the starting point of oxygen content to be at high place.

On the basis that the oxygen content is negatively correlated to annealing temperature, we decided to lower the annealing temperature in nitrogen atmosphere to the 500 ℃ to approach the target value, 0.5. The oxygen content variation x at thermodynamic equilibrium is titrated to be about 0.52 this time, quite close to the target. So next we slightly raised the annealing temperature attempting to 515 ℃ and later 510 ℃ eliminate the excess oxygen of 0.02. The result was improved a little bit, same as expected. Finally, we were able to establish the right annealing condition: 515 ℃ or 510℃ in nitrogen atmosphere with enough annealing time over 12 hours.

Table 3. Oxygen content variation (x_n) before and after annealing. T stands for annealing temperature, and t for annealing time. “At.” column is for the atmosphere, including nitrogen

with gas flow was around 60ml/h, and air in a closed system. The titration was repeated, denoted as x_1, x_2 and x_3.

Initial x value	Annealling condition			Titration after annealing		
x_0	T (°C)	t (hour)	At.	x_1	x_2	x_3
as-synthesized				0.7428	0.7411	0.7433
0.7424	900	12	N_2	0.3674	0.367	0.3748
0.7424	900	12	N_2	0.7042	0.6913	0.6996
0.7424	900	12	N_2	0.6603	0.7153	0.6993
0.7424	900	12	N_2	0.2001	0.2081	0.2087
0.7424	900	8	N_2	0.1748	0.175	0.1749
0.7424	900	8	N_2	0.1868	0.1829	0.2266
0.2056 & 0.1749 & 0.1988	1100	24	Air	0.7076	0.7037	
0.7057	1100	24	Air	0.7061	0.7008	0.7015
0.7424	500	10	N2	0.5143	0.5216	0.5199
0.7424	515	11.5	N2	0.537	0.5389	0.5352
0.7057	515	11.5	N2	0.5217	0.5213	0.5159
0.7424	515	11.5	N2	0.4875	0.4856	0.491
0.537	515	11.5	N2	0.4898	0.491	0.4944
0.5196	515	11.5	N2	0.4895	0.4865	0.4919
0.7061	510	24	N2	0.5185	0.5114	0.5134
0.4880 & 0.4917 &0.4893	510	24	N2	0.5242	0.5224	0.5232
0.5144 & 0.5233	510	8	N2	0.5078	0.4996	0.5072

2.3.3 Synthesis of Bulk-Form $PrBaCo_2O_{5+x}$

In the later stage of this project, we realized that it is necessary to expand our study of $PrBaCo_2O_{5.5}$ to those with other oxygen contents. In order to measure the resistivity, samples in bulk form are also necessary, but it may cause the inhomogeneity during annealing process. We tried various conditions on both powder and bulk sample in a small amount to search for the best synthesis condition, and simultaneously carried out the examination of the homogeneity by titrate the edge part, inside core part of the bulk and powder form respectively. The powder-form sample was set as a reference because of its good homogeneity.

Table 4. Oxygen content variation (x_n) before and after annealing in nitrogen atomosphere. T stands for annealing temperature, and t for annealing time, nitrogen gas flow is around 60ml/h. Titration was repeated, denoted as x_1, x_2 and x_3.

Initial x value	Annealling condition		Titration after annealing			
x_0	T (°C)	t (hour)	Sample form	x_1	x_2	x_3
			Powder	0.5201	0.5159	0.5114
0.663	515	12	Bulk(Whole)	0.5062	0.5051	0.5251
			Bulk(Core)	0.5251		
0.735	300	14	Powder	0.6762	0.666	0.6641
			Powder	0.1975	0.1961	0.193
0.735	900	17	Bulk(Edge)	0.1961	0.1974	
			Bulk(Core)	0.1893	0.1992	0.188
0.735	400	17	Powder	0.5982	0.6001	0.5938
			Powder	0.5536	0.5682	
0.735	450	20	Bulk(Edge)	0.5521	0.5501	
			Bulk(Core)	0.5416	0.5474	

As shown in Table 4, the powder and the bulk contain almost the same amount of oxygen, although powder generally has a little bit more. However, a small difference (about 0.01) exists between the core part of bulk and edge part. So we decided to extend the annealing time to 40 hours and in 400 °C and 600 °C (Table 5). The experiment in 400 °C failed because of the running out of the nitrogen gas during annealing without notice. Finally, more homogeneity was achieved by the bulk at 600 °C. Taking into account of heating time (about 6 hours) and cooling time (about 12 hours), it will take 3 days to get one sample, which is too long in our consideration. Thus, annealing in shorter time was tried with simultaneously changing to the annealing temperatures, such as 700 °C and 450 °C, as shown in Table 5. It was found that the oxygen content variation by 25 hours is almost in the identical level as that by 40 hours, illustrating that 25-hour annealing is fairly enough to achieve the homogeneity.

Table 5. Oxygen content variation (x_n) before and after annealing in nitrogen atomosphere. T stands for annealing temperature, and t for annealing time, nitrogen gas flow is around 60ml/h.

Titration was repeated, denoted as x1, x2 and x3.

Initial x value	Annealing condition		Titration after annealing		
x_0	T (°C)	t (hour)	Sample form	x1	x2
			Bulk(Edge)	0.5625	0.5598
0.735	400	47(imperfect N2)	Bulk(Core)	0.5466	0.5572
			powder	0.4518	0.4505
0.735	600	40	Bulk(Edge)	0.4485	0.4467
			Bulk(Core)	0.4487	0.4488
			powder	0.3562	0.3611
0.735	700	33	Bulk(Edge)	0.3549	0.3576
			Bulk(Core)	0.3707	0.3690
			powder	0.5575	0.5603
0.7059	450	25	Bulk(Edge)	0.5467	0.5512
			Bulk(Core)	0.5454	0.5410

On determining the annealing time, samples of large amount were synthesized at each annealing temperature, listed in Table 6. A large range of oxygen content were successfully obtained, with x value varies from 0.18 to 0.735.

Table 6. Oxygen content variation (x_n) before and after annealing in nitrogen atomosphere. T stands for annealing temperature, and t for annealing time, nitrogen gas flow is around 60ml/h. Titration was repeated, denoted as x1, x2 and x3.

Initial x value	Annealing condition		Titration after annealing		
x_0	T (°C)	t (hour)	Sample form	x1	x2
			Bulk(Edge)	0.1798	0.1802
0.7059	900	25	Bulk(Core)	0.1802	0.1803
			Bulk(Edge)	0.5124	0.5094
0.7059	515	25	Bulk(Core)	0.5080	0.5066
			Bulk(Edge)	0.5668	0.5668
0.7059	400	25	Bulk(Core)	0.5645	0.5637
			Bulk(Edge)	0.6050	0.6106
0.7059	350	25	Bulk(Core)	0.5962	0.5979
			Bulk(Edge)	0.6520	0.6465
0.7059	300	25	Bulk(Core)	0.6417	0.6456
			Bulk(Edge)	0.4594	0.4518
0.7059	600	25	Bulk(Core)	0.4445	0.4436

			Bulk(Edge)	0.3349	0.3396
0.7059	700	25	Bulk(Core)	0.3295	0.3341

2.3.4 Synthesis of Oxygen Disordering

The stoichiometric $PrBaCo_2O_{5.5}$ synthesized above is with the oxygen vacancy ordering in Pr layer, which makes the alternative pyramidal and octahedral coordinations along b axis, resulting in a divergence of lattice constant a and b. Effort were also made to synthesize the $PrBaCo_2O_{5.5}$ with disordering oxygen distribution, by quick annealing and then quenching. However, even tried various conditions, as shown in Table 7, the featuring (4 0 0) and (0 4 0) peaks in unit cell ($2a_p \times 2a_p \times 2a_p$) remain splitting from XRD characterization (Fig. 6), illustrating that the oxygen disordering sample fails to be obtained in this way.

Table 7. Oxygen content (x_n) before and after annealing. T stands for annealing temperature, and t for annealing time, gas flow is around 60ml/h.

Initial x value	Annealing condition			Titration after annealing	
x_0	T(°C)	t(h)	Quench	Sample form	x_1
				Bulk(Edge)	0.6833
0.7059	600	0.5	in water	Bulk(Core)	0.6815
0.7059	600	1	in water	whole	0.4807
0.7059	600	0.8	in water	whole	0.4915
0.7059	600	1	in water	whole	0.4835
0.7059	600	0.7	open furnace	whole	0.7459
0.7059	515	2	in water	whole	0.5471

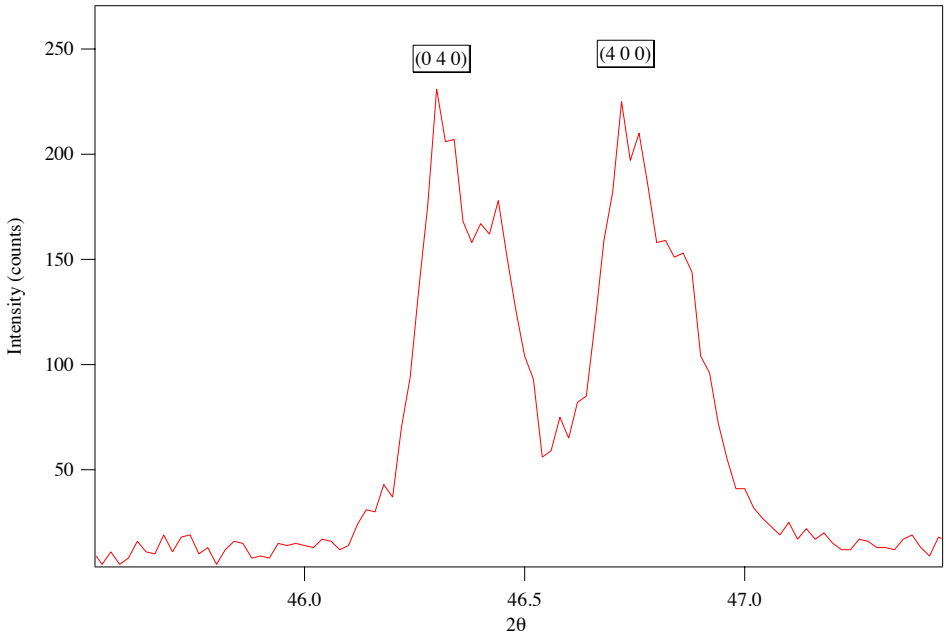

Fig. 6 XRD pattern of sample synthesized by annealing at 515 °C for 2 hours and quenched in the water.

Chapter 3 Structural and Physical Properties

3.1 Structure Characterization

3.1.1 Diffraction

Crystals are made of atoms, ions or groups of atoms repeated along the three dimensions to form a three dimensional lattice. Diffraction, simplified for “Bragg Diffraction”, occurs when coherent electromagnetic radiation or subatomic particle waves are scattered by the atoms in a crystalline system with wavelength comparable to atomic spacings, undergoing constructive interference in accordance to Bragg's law. As schematically shown in Fig.7, two beams with identical wavelength and phase approach a crystalline solid and are scattered off two different atoms within it. The lower beam traverses an extra length of $2d\sin\theta$. Constructive interference occurs when this length is equal to an integer multiple of the wavelength of the radiation, i.e., $n\lambda = 2d\sin\theta$, known as Bragg law, where n is an integer, λ is the wavelength of incident wave, d is the spacing between the planes in the atomic lattice, and θ is the angle between the incident ray and the scattering planes. Very strong intensities known as Bragg peaks are obtained in the diffraction pattern when scattered waves satisfy the Bragg law. In other words, the peak position only depends on the lattice parameters of the crystal a, b, c, α, β and γ.

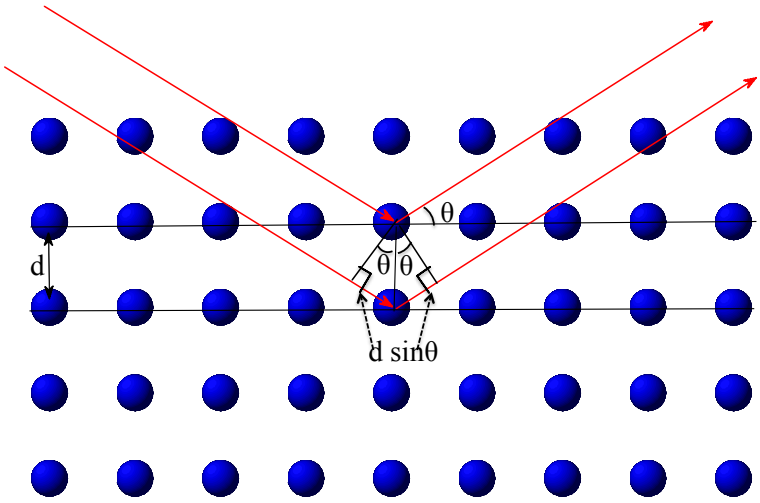

Fig. 7 Schematic illustration of Bragg law.

Another aspects should be considered when dealing with diffraction patterns: the intensity of the diffracted beams, which is associated with the positions of the atoms in the unit cell. Therefore, combining the information both positions and intensities of Bragg peaks will allow us to determine the crystal structure.

Two kinds of diffraction methods are commonly used for studying the crystal structure, e.g., single crystal diffraction and powder diffraction. There is little doubt that single crystal diffraction are superior for ab initio structure solution since it provides a direct three dimensional information. However, the requirement of large size of single crystal imposes tremendous difficulty to the application of this technique to the compounds, because a large majority of the materials of interest in physics, materials science, and many in solid state chemistry are not readily available in single crystal form. Moreover, many functional materials are intrinsically highly twinned or deliberately mult-phase. As the feasibility of determination of crystal structure by powder diffraction has significantly improved in recently years, structural analysis of compounds prepared in microcrystalline powders resides in an important position with utmost number of users.

3.1.2 X-ray Powder Diffraction (XRD)

Since the repeat distances in these crystal lattices are about 0.2 nm, diffraction by visible light (with a wavelength λ in the range 350 to 700 nm) is impossible. X rays are electromagnetic waves like visible light but they have a much shorter wavelength in the same range than the crystal repeat distances so that they can be diffracted.

Two X-ray powder diffractometers were used for the structure characterization on the powder crystalline samples. One is the Rigaku D/Max 2000 diffractometer using Cu $K\alpha_1\alpha_2$ radiation (λ = 1.542 Å) from the rotating anode generator (40 kV, 100 mA), and another is Rigaku SmartLab diffractometer using Cu $K\alpha_1\alpha_2$ radiation (λ = 1.542 Å) from the sealed tube generator (30 kV, 40 mA). The data for phase identification were collected in Rigaku D/Max 2000 in continuous scanning mode with a speed of 8° per minute. The data for structure refinement were collected by both diffractometers in step scanning mode with the increment of 0.02° and a counting time of 6 s per step for Rigaku D/Max 2000 (35 s per step for Rigaku SmartLab) at room temperature (25 °C). The high temperature XRD were performed by a combination of Rigaku SmartLab and Anton Paar HTK 1200N High-Temperature Oven Chamber, using step scanning with the increment of 0.02° and a counting time of 40 s per step in the temperature range of 25 - 100 °C. The diffraction data were analyzed by Rietveld refinement with the Z-Rietveld program in a software suit, Z-Code [43–45].

3.1.2 Neutron Powder Diffraction

The fact that neutrons interact with the nuclei while X-ray or electrons interact with electrons makes neutron powder diffraction complementary to X-ray diffraction and electron microscopy. The sensitivity to element for X-ray or electron scattering is just positively correlated to the atomic number, so that it is hard for them to probe light elements, particularly hydrogen. Neutron has no systematic dependence on atomic number and it turns out that its sensitivity to many light elements, such as hydrogen, oxygen etc. is fairly high. For example, in this thesis,

neutron powder diffraction played an important to precisely determine the oxygen position and concentration when X-ray or electron diffraction fails in this task. However, because of this and the large capital costs associated with intense neutron sources, neutron diffraction is rarely the first technique used to study a particular material. More often, a range of samples have already been studied using other techniques and neutron diffraction is used in a highly specialization way to provide critical information.

Neutron powder diffraction was carried out at room temperature, using SuperHRPD, the high resolution neutron power diffractometer installed at the pulsed spallation neutron source of Japan Proton Accelerator Research Complex (J-PARC) in Tokai, Japan. The data were collected by detectors of the back scattering bank in order to achieve a high resolution. The back scattering bank covers a 2θ range of 150 - 175°, corresponding to d-spacing range of 0.3 - 4.0 Å. The best resolution (Δd/d) of 0.035% can be achieved at 2θ of 175°. In this study all the signals of the bank are focused to 172° by the time focusing method. The diffraction data were analyzed by Rietveld refinement with the Z-Rietveld program in a software suit, Z-Code for crystal structure [43–45]. A new type of peak shape function optimized for time-of-flight diffraction pattern, so called "Type 0" profile function, was adopted for the refinement. As for magnetic structure, symmetry analysis was performed with two softwares, BasIreps in the FullProf Suite package [46], and SARAh [47], and the Rietveld refinement for magnetic structure was conducted using the FullProf Suite package [46].

3.1.3 Electron Diffraction

Despite very strong similarities with X-ray and neutron diffraction, electron diffraction displays some specificities, which to a large extend, are due to the interactions of the incident electrons with the specimen and to the electron wavelength. Thus, the electron cross sections are 10^4 to 10^5 times larger than the ones for X rays and neutrons meaning that the interactions of electrons with a crystal are very strong. As a result, the diffracted beams can have a large intensity and interact. This behavior is interpreted with the complex dynamical theory while X-ray and

neutron diffractions are more simply described with the kinematical theory. These strong interactions have some advantages: it is possible to obtain electron diffraction patterns from very tiny diffracted volumes (in the range $1nm^3$ to $1\mu m^3$) even after very short exposure times (a few seconds). They also have some disadvantages. The main one concerns the specimens; they must be thin enough to be crossed by electrons and this is a serious limitation. Moreover, large relaxations of the diffraction conditions are observed with thin crystals meaning that diffraction occurs in a more or less large angular domain around the Bragg angles and not only at the precise Bragg angles as it is the case with X rays and neutrons.

Electron diffraction patterns were taken on JEOL JEM-2100 transmission electron microscope, with and accelerating voltage of 200kV and a camera length between 250 and 400 mm. The JEM-2100 features a high-stability goniometer stage specifically tuned for high tilt tomographic applications. The optional JEOL TEMography™ software system automatically acquires and registers images, automatically calculates the 3-D reconstruction, and provides 3-D visualization software to display and rotate the image on a variety of axes. An x/y piezo stage is an available option.

3.2 Specific Heat

The specific heat was measured in the temperature range between 20 and 100 °C by The STA 449 F3 Jupiter, which comprises a robust system for high-quality Thermogravimetry (TGA) and (Differential Scanning Calorimetry) DSC measurements. The resolution of this low-drift balance system is 1 µg.

Differential scanning calorimetry (DSC) monitors heat effects associated with phase transitions and chemical reactions as a function of temperature. In a DSC the difference in heat flow to the sample and a reference at the same temperature, is recorded as a function of temperature. The reference is an inert material such as alumina, or just an empty aluminum pan. The temperature of both the sample and reference are increased at a constant rate. Since the DSC is at constant pressure, heat flow is equivalent to enthalpy changes:

$$\left(\frac{dq}{dt}\right)_p = \frac{dH}{dt} \tag{2}$$

Here dH/dt is the heat flow measured in mcal/sec. The heat flow difference between the sample and the reference is:

$$\Delta\frac{dH}{dt} = \left(\frac{dH}{dt}\right)_{sample} - \left(\frac{dH}{dt}\right)_{reference} \tag{3}$$

and can be either positive or negative.

The first and most direct information obtainable from a DSC curve is the temperature at which a certain process occurs, for example, the phase transition point. The temperature at which a reaction, such as decomposition, may start is another important parameter. The peak temperature is associated with the temperature at which maximum reaction rate occurs.

The second direct information is the enthalpy associated with certain processes, such as specific heat and changes in heat capacity. The specific heat is defined as:

$$C_p = \left(\frac{dq}{dT}\right)_p = \left(\frac{dH}{dT}\right)_p = \frac{dH}{dt}\frac{dt}{dT} \tag{4}$$

where dT/dt is the temperature is the scan rate. For differential measurements, we determine the difference in the specific heat of the sample and the reference:

$$\Delta C_p = \Delta(\frac{dH}{dT})_p = \Delta \frac{dH}{dt}\frac{dt}{dT} = (C_p)_{sample} - (C_p)_{reference} \quad (5)$$

When is specific heat of the reference is known, the specific heat of the sample can be derived from Equation 5.

3.3 Magnetic and Transport Properties

3.3.1 Magnetization

Magnetization measurements were performed using a superconducting quantum interference device (SQUID) magnetometer (Quantum Design model MPMS) in direct current (DC) mode with the temperature range between 10 and 400 K.

A SQUID is a very sensitive device available for measuring magnetic fields. Although the SQUID in the MPMS is the source of the instrument's remarkable sensitivity, it does not detect directly the magnetic field from the sample. Instead, the sample moves through a system of superconducting detection coils which are connected to the SQUID with superconducting wires, allowing the current from the detection coils to inductively couple to the SQUID sensor. When properly configured, the SQUID electronics produces an output voltage which is strictly proportional to the current flowing in the SQUID input coil. Therefore, the thin film SQUID device, which is located approximately 11 cm below the magnet inside a superconducting shield, essentially functions as an extremely sensitive current-to-voltage convertor.

A measurement is performed in the MPMS by moving a sample through the superconducting detection coils, which are located outside the sample chamber and at the center of the magnet. As the sample moves through the coils, the magnetic moment of the sample induces an electric current in the detection coils. Because the detection coils, the connecting wires, and the SQUID input coil form a closed superconducting loop, any change of magnetic flux in the detection coils produces a change in the persistent current in the detection circuit, which is proportional to the change in magnetic flux. Since the SQUID functions as a highly linear current-to-voltage convertor, the variations in the current in the detection coils produce corresponding variations in the SQUID output voltage which are proportional to the magnetic moment of the sample. In a fully calibrated system, measurements of the voltage variations from the SQUID detector as a

sample is moved through the detection coils provide a highly accurate measurement of the sample's magnetic moment. The system can be accurately calibrated using a small piece of material having a known mass and magnetic susceptibility.

3.3.2 Resistivity

Resistivity was measured by a standard ac four-probe method using the Quantum Design Physical Property Measurement System (PPMS) in the temperature range between 10 and 400 K. To ensure good electric contacts, thin gold wires were attached to the contact pads using a room-temperature-drying gold paste, which electrically and mechanically bound the wire to the sample.

Four-probe method is an electrical impedance measuring technique that uses separate pairs of current-carrying and voltage-sensing electrodes to make more accurate measurements than traditional two-terminal (2T) sensing. In typical four-probe measurements, 4 electrical leads are attached to a rectangular sample along a straight line (Fig. 8). A current is fed from contact A to contact B, and the voltage is measured across contacts C and D, which must be far away from the current contacts in order for the lines of current flow to be uniform and parallel between C and D. The resistivity of the sample can be derived from the voltage drop across contacts C and D, the applied current, and the geometry of the sample. Using four probes eliminates measurement errors due to the probe resistance, the spreading resistance under each probe, and the contact resistance between each metal probe and the semiconductor material. Because a high impedance voltmeter draws little current, the voltage drops across the probe resistance, spreading resistance, and contact resistance are very small.

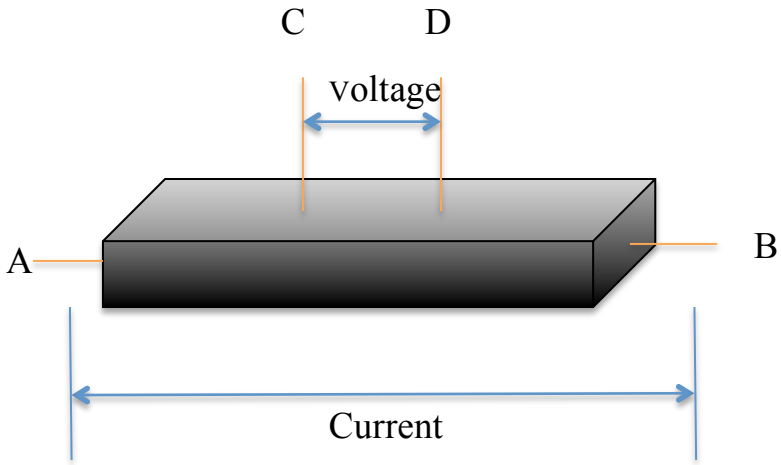

Fig. 8 Schematically illustration of four-probe resistivity measurement

3.4 Electronic State

3.4.1 X-ray Photoemission Spectroscopy (XPS)

X-ray Photoelectron Spectroscopy (XPS), also known as X-ray Photoemission Spectroscopy, is one of the most powerful surface analytical techniques capable to provide accurate qualitative elemental analysis, quantitative composition and, simultaneously determination of the chemical state (binding and oxidation) is also straightforward. The information is originated from the top ~10 nm surface layer (with the customary excitation energies). The applied soft X-ray excitation, in most of the cases is not destructive for the surface. In XPS process, a core electron is exited by the incident X-ray to the high-energy continuum states and detected as a photoelectron.

In the historical development of the study of XPS, the one-electron excitation was first taken into account, and after that many-body effects were widely studied. Within the one-electron approximation, the kinetic energy ε of the photoelectron is determined by the energy conservation law:

$$\varepsilon = \hbar\Omega - (\varepsilon_F - \varepsilon_c) - \phi \tag{6}$$

where $\hbar\Omega$ is the incident photon energy, ε_c the core level, ε_F the Fermi level, and ϕ is the work function. Theoretically, ε_c is obtained by the Hartree-Fock approximation, and then Equation 6 represents the Koopmans' theorem. Experimentally, on the other hand, the value of ε_c can be estimated from the XPS spectrum if the other quantities of Equation 6 are known. Since the value of ε_c is not very much away from the corresponding value of the free atom, which is fairly different between elements, XPS is useful for the analysis of elements in solid. The small deviation of ε_c from that of the free atom, denoted by the chemical shift, provides us with the information on the chemical bonding of valence electron states, allowing us to analyze the chemical state of the ions or molecules.

However, Koopman's theorem does not generally hold because of the many-body effect beyond the one-electron approximation. When the core hole is created in the XPS process, valence electron states are polarized by the core hole electron and screen it. This polarization occurs with charge-transfer effect. Due to the progress in experimental techniques, the many-body charge-transfer effect in XPS can be observed as an asymmetry of the spectral shape and as satellite peaks in various materials, providing us the essential information of electronic states. For example, the satellites nowadays plays an important role in identifying the atom's chemical state as in many case the chemical shift are too small to distinguish the chemical state.

The XPS data were taken on an AXIS-Ultra instrument from Kratos Analytical using monochromatic Al Kα radiation (225 W, 15 mA, 15 kV) and low–energy electron flooding for charge compensation. The chamber pressure was less than 5.0×10^{-9} Torr. To compensate for surface charges effects, binding energies were calibrated using C 1s hydrocarbon peak at 284.80 eV.

3.4.2 Soft X-ray Absorption Spectroscopy (XAS)

Soft X-ray Absorption Spectroscopy (XAS) is a widely used technique for determining the local geometric and/or electronic structure of matter. The experiment is usually performed at synchrotron radiation sources, which provide intense and tunable X-ray beams. Samples can be in the gas-phase, solution, or condensed matter (i.e. solids). In XAS process, a core electron is excited near to the excitation threshold, which corresponds to the conduction band. As a result, much information about the unoccupied state, i.e., density of states, can be extracted from the XAS spectra. Unique to soft x-ray absorption is that the dipole selection rules are very effective in determining which of the final states can be reached and with what intensity, starting from a particular initial state. This makes the technique extremely sensitive to the symmetry of the initial state, i.e., the valence, orbital, and spin states of the ion.

The many-body charge-transfer effect, commonly observed in XPS, is much weaker in XAS

spectra. The physical reason for the weaker charge-transfer effect in XAS is the screening of the core hole potential by the photo-excited electron, which stays in the bonding states and directly participates with the screening of the core hole potential, thus suppressing a further screening by the charge-transfer effect in going from intial to final states of XAS. On the other hand, in XPS, a core electron is exited to the high-energy continuum to be detected as a photoelectron and never participate in the screening of the core hole potential.

XAS were performed in a synchrotron-based soft x-ray beamline, BL-16A, of the Photon Factory in High Energy Accelerator Research Organization, Japan. The beamline was constructed in order to investigate magnetism and surface chemistry by using the X-ray spectroscopies with circularly and linearly polarized soft X rays. The beamline was designed to cover the energy range 200–1500 eV, with resolving power, $E/\Delta E$, 5000-10000 in the whole energy range, by adopting an APPLE-II type undulator and a variable-included-angle Monk-Gillieson mounting monochromator with varied-line-spacing (VLS) plane gratings. Spectroscopic measurements were carried out total electron yield (TEY) mode using soft x rays in the vicinity of the Co $L_{2,3}$ (780–800 eV) and O K (528–535 eV) absorption edges.

Chapter 4 Data Analysis & Discussion

4.1. Temperature induced Metal-Insulator Transition (MIT) for stoichiometric $PrBaCo_2O_{5.5}$

4.1.1. Resistivity and Inverse magnetic susceptibility

$PrBaCo_2O_{5.52}$ was adopted for this study, the oxygen content of which was first measured by iodometric titration and later revised by Rietveld refinement on neutron powder diffraction data. MIT occurs at about 346 K [Fig. 9 (a)], defined as T_{MI}, accompanied by an anomaly in inverse magnetic susceptibility [Fig. 9 (b)]. Hereafter, we define $T < T_{MI}$ as insulating phase and $T < T_{MI}$ as metal phase. It should be noted that even above the T_{MI}, the temperature dependence of the resistivity still behaves like a semiconductor.

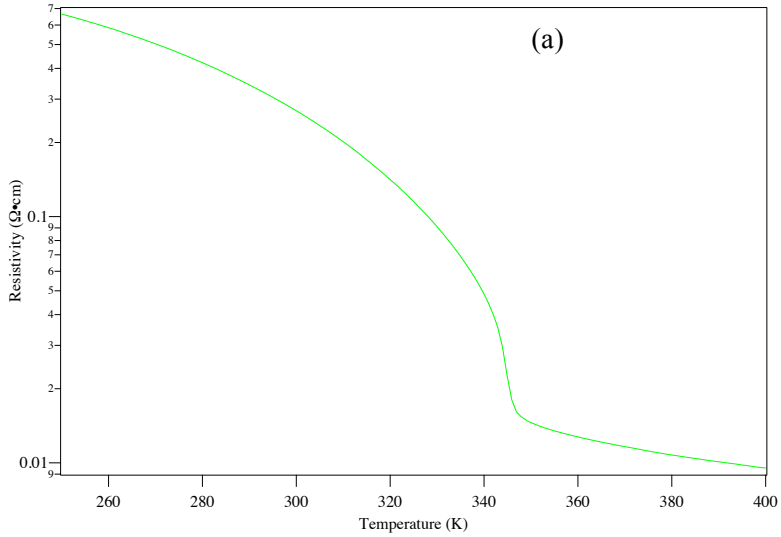

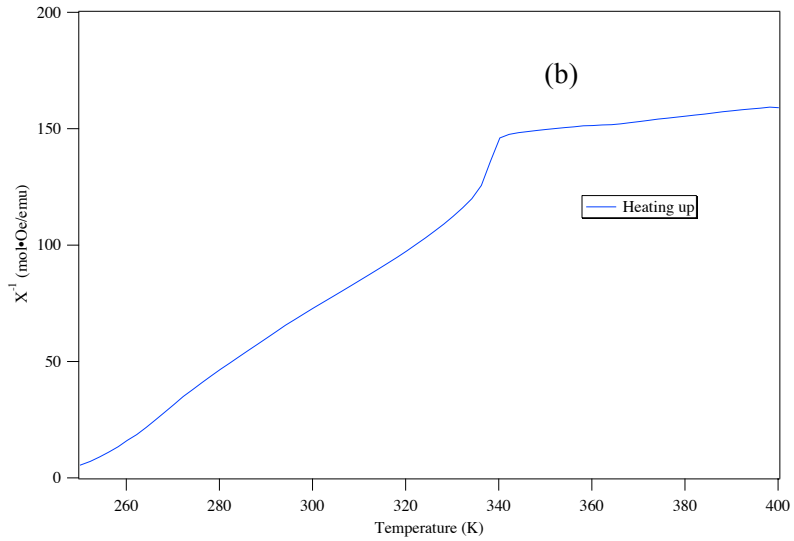

Fig. 9 (a) Temperature dependence of resistivity ρ of $PrBaCo_2O_{5.52}$ (b) Inverse susceptibility 1/X of $PrBaCo_2O_{5.52}$ measured under a field of 100 Oe after cooling down to 10 K in the zero field (ZFC).

4.1.2. Crystal structure

The crystal structure was studied by the combination of three diffraction techniques, that is electron diffraction, X-ray powder diffraction and neutron powder diffraction. The key to distinguish Pmmm ($a_p \times 2a_p \times 2a_p$) and Pmma ($2a_p \times 2a_p \times 2a_p$) is the super lattice peaks arising from the doubling of a axis, which have never been observed by neutron diffraction before. Possessing the feature of high resolution and low background, the room temperature neutron powder diffraction experiment by SuperHRPD enables us to observe super lattice peaks along a axis, such as (3/2 1 1), (1/2 3 1), (3/2 0 1) etc., indexed by the $a_p \times 2a_p \times 2a_p$ unit cell, as shown in Fig. 10(a). It is the first time to see such super lattice peaks from neutron diffraction pattern, and we speculate the reason that other neutron diffractometers, such as those in Ref. [23,25,26], could not find the super lattice peaks is due to the relative high background of the diffractometers, because the integrated intensity for the strongest super lattice peak (1/2 3 1) observed by SuperHRPD is only about 0.5% of that for the strongest reflection (1 2 2) in the pattern [Fig. 10(b)].

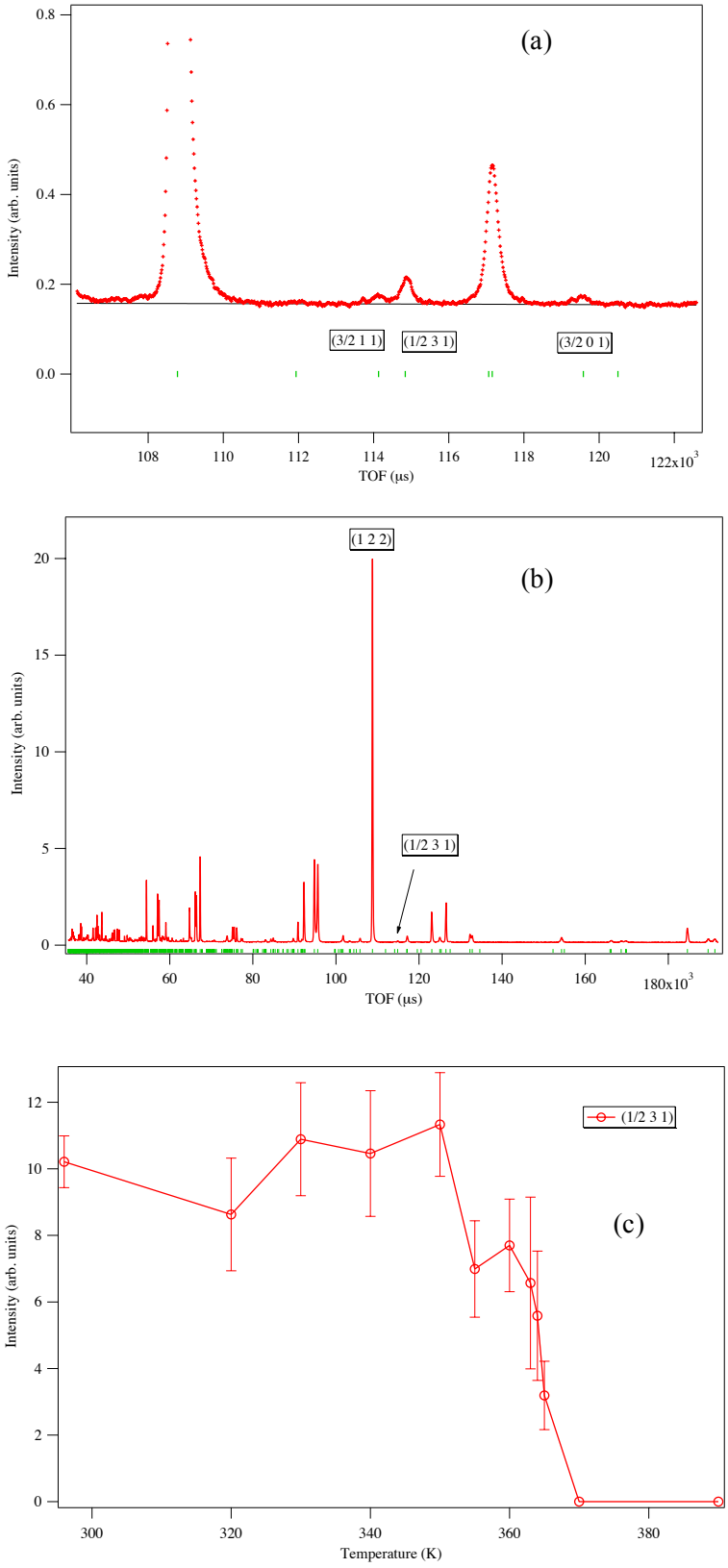

Fig. 10 Neutron powder diffraction of $PrBaCo_2O_{5.52}$ at room temperature by SuperHRPD (a) Supper lattice peaks (3/2 1 1), (1/2 3 1) and (3/2 0 1) indexed (green bars) by unite cell ($a_p \times 2a_p \times 2a_p$) (b) Full pattern, green bars are the indices by ($a_p \times 2a_p \times 2a_p$) (c) Temperature dependence of intensity of the (1/2 3 1) super lattice reflection.

Electron diffraction provides another evidence for the super lattice. By measuring the q-spacing in electron diffraction pattern, the corresponding d-spacing in real space can be obtained. In this way the spots can be indexed by referring to the lattice constant determined by x-ray or neutron powder diffraction. As demonstrated in Fig. 11, two combinations of indices with close d-spacing can be assigned to the reflections marked by rectangle and circle in the framework of $a_p \times 2a_p \times 2a_p$ unit cell: (1/2 0 1) for rectangle, (0 1 0) for circle; or (0 1 1) for rectangle, (1/2 0 0) for circle. In either case, super lattice along a axis must occur.

Thus, with the super lattice reflections from both neutron powder diffraction and electron diffraction, it is easy to conclude the crystal structure for the insulating phase is Pmma ($2a_p \times 2a_p \times 2a_p$), confirming the model constructed based on super lattice reflections observed by single crystal x-ray diffraction [31–33].

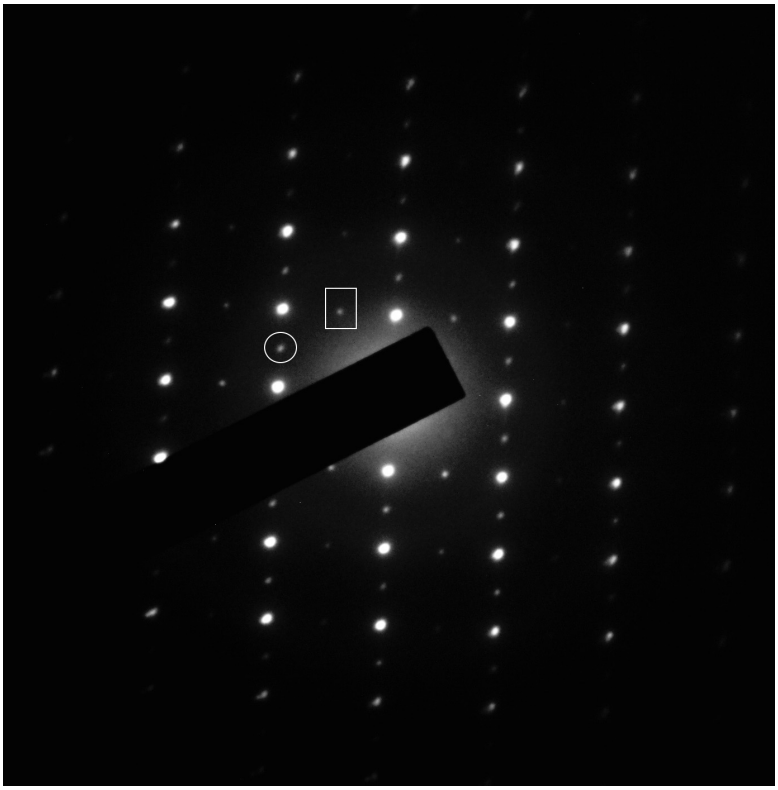

Fig. 11 Electron diffraction pattern of $PrBaCo_2O_{5.52}$ at room temperature. Two combinations of indices with close d-spacing can be assigned to the reflections marked by rectangle and circle in the framework of $a_p \times 2a_p \times 2a_p$ unit cell: (1/2 0 1) for rectangle, (0 1 0) for circle; or (0 1 1) for rectangle, (1/2 0 0) for circle. Multiple scattering was checked during the measurement.

The temperature dependence of (1/2 3 1) peak [Fig. 10(c)] clearly demonstrates a structure phase transition from Pmmm ($a_p \times 2a_p \times 2a_p$) to Pmma ($2a_p \times 2a_p \times 2a_p$) cooling across the the MIT temprature. It should be noted that the displaying temperature in Fig. 10(c) is not the real sample temperature because of the temperature gradient between the thermocouple and the sample or possibly the incorrect calibration of the thermocouple. The actual structure transition temperature (T_S) is the same as the MIT temperature T_{MI}, which is justified by the XRD measurement. Fig. 12(a) shows part of the XRD pattern, the temperature evolution of (0 4 0) and (4 0 0) bragg peaks indexed by the $2a_p \times 2a_p \times 2a_p$ unit cell, where T_S is determined to be 345K, just 1K different from the T_{MI} from resistivity measurement.

4.1.3. First order phase transition

At first glimpse of the Fig. 12(a), the structure phase transition seems to be the second order phase transition. However, if we look carefully in to pattern, we will find that in the critical region (335K to 345K) the observed intensity (the height of the peak) is dampened down. This feature is more clearly shown in the three-dimensional diagram, Fig. 12(b). Since the peak damping is often observed in the first order phase transition, it is necessary to further identify the order of the phase transition with more clear evidence. A lambda type curve of specific heat is observed [Fig. 12(c)], which is generally interpreted as the first order phase transition. Also, by the high resolution neutron diffraction, we observed the presence of splitting of (0 0 4) and (4 0 0) peaks in the narrow critical region [Fig. 12(d)], a rigorous proof of co-existing phases, which is another typical feature of the first order phase transition. Therefore, a conclusion of first order structure phase transition can be drawn from these experimental results.

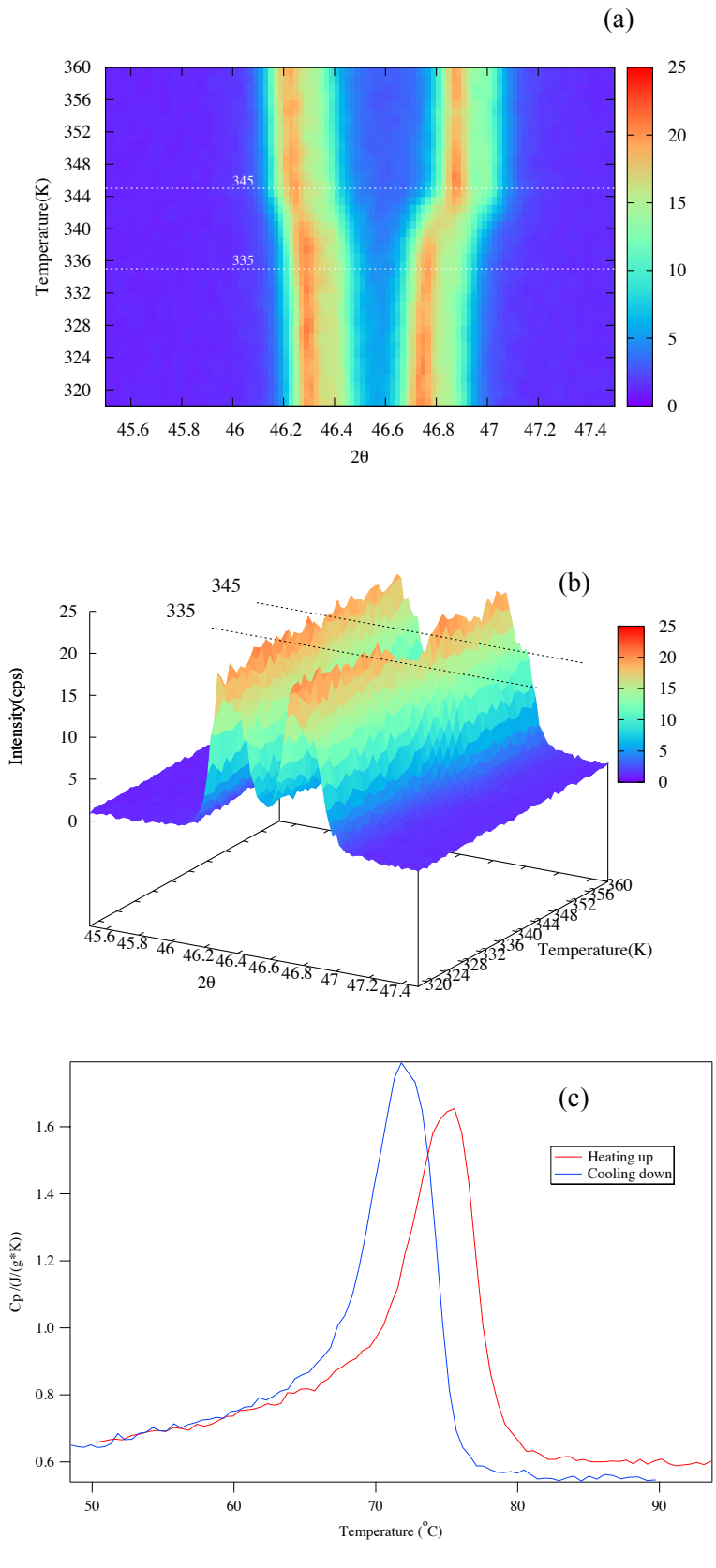
(a)
Temperature(K)
2θ
345
335
(b)
Intensity(cps)
Temperature(K)
2θ
(c)
Heating up
Cooling down
Cp /(J/(g*K))
Temperature (°C)

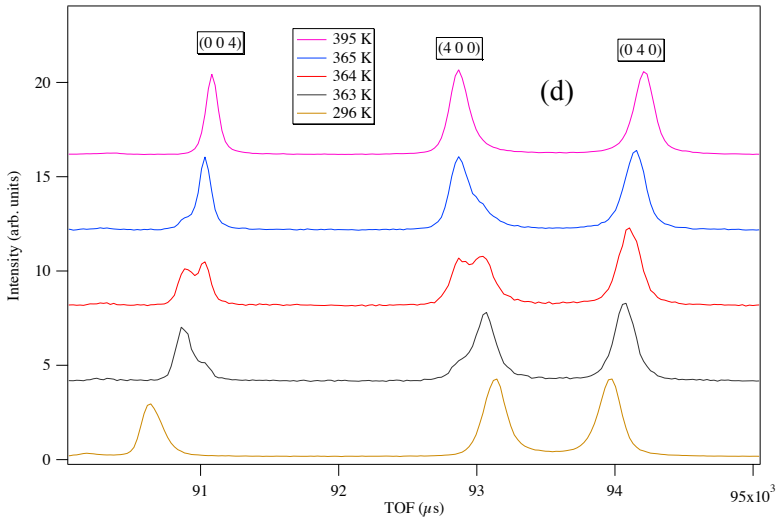

Fig. 12 [a, b] XRD temperature scan of $PrBaCo_2O_{5.52}$ (a) 2-D diffraction pattern; the intensity are demonstrated by the color, from red (strong) to blue (weak);the two red arrows indicates the critical region; the bragg peaks are indexed by the $2a_p \times 2a_p \times 2a_p$ unit cell. (b) 3-D ifrraction pattern; the intensity are demonstrated by the color, from red (strong) to blue (weak); the two red lines indicates the critical region (c) Specific heat curve of $PrBaCo_2O_{5.52}$ in both heating and cooling process. (d) Neutron powder diffraction temperature scan of $PrBaCo_2O_{5.52}$, the bragg peaks are indexed by the $2a_p \times 2a_p \times 2a_p$ unit cell.

4.1.4. Charge ordering or Spin state transition

Through Rietveld refinement, the crystal structure parameters for both metal phase and insulator phase were determined, as listed in Table 8 and Table 9, respectively. The resultant Co-O bond lengths are shown in Table 10 and Table 11. As we can see, the pyramidal site in metal is split into two non-equivalent pyramidal sites in insulator phase, so are the octahedral sites. The splitting manifests itself in the average Co-O bond lengths, where Co(Pyr)-O splits from 1.940 into 1.938 and 1.957, Co(Oct)-O from 1.987 into 1.942 and 2.007. If we look at the insulator phase, the difference of average Co-O bond length between the two pyramids is about 0.02 Å while between the two octahedra are over 0.06 Å. Discrepancy of 0.06 Å in the bond length are quite large that it may indicate the presence of charge ordering. And in the case of Co^{3+}, the polyhedron size can vary upon the spin states, since LS Co^{3+} ions do not have e_g electrons compared with IS or HS Co^{3+} ions. So the spin state ordering can also lead to such a large

difference.

Table 8. Crystal structure parameters, including occupancy, atomic coordinates, and displacement parameters, determined for $PrBaCo_2O_{5.52}$ sample at T=395 K from the neutron powder diffraction data, using orthorhombic space group Pmmm ($a_p \times 2a_p \times 2a_p$). The lattice constant and the criteria of the Rietveld refinement quality are: a= 3.89832(1) Å, b= 7.90892(2) Å, c= 7.64649(2) Å; Rwp=9.54%.

Atom	Occupancy	x	y	z	100U
Ba	1	0.5	0.2485(1)	0	0.63(2)
Pr	1	0.5	0.2680(1)	0.5	1.45(3)
Co1	1	0	0.5	0.2502(2)	0.94(4)
Co2	1	0	0	0.2513(2)	0.75(3)
O1	1	0	0	0	1.63(3)
O2	1	0	0.5	0	0.95(3)
O3	0.912(3)	0	0.5	0.5	0.94(4)
O4	0.142(3)	0	0	0.5	0.94(4)
O5	1	0.5	0	0.3041(1)	1.79(2)
O6	1	0.5	0.5	0.2653(1)	1.46(2)
O11	1	0	0.2374(1)	0.2876(1)	1.50(2)

Table 10. Crystal structure parameters, including occupancy, atomic coordinates, and displacement parameters, determined for $PrBaCo_2O_{5.52}$ sample at T=296 K from the neutron powder diffraction data, using orthorhombic space group Pmma ($2a_p \times 2a_p \times 2a_p$). The lattice constant and the criteria of the Rietveld refinement quality are: a = 7.81807(3) Å, b = 7.88734(3) Å, c = 7.60911(2) Å; R_{wp}=8.70%.

Atom	Occupancy	x	y	z	100U
Ba	1	0	0.2509(1)	0	0.28(1)
Pr	1	0	0.2695(1)	0.5	0.69(1)
Co1	1	0.25	0	0.2473(3)	0.66(4)
Co2	1	0.75	0	0.2553(3)	0.33(4)
Co3	1	0.25	0.5	0.2517(3)	0.15(4)
Co4	1	0.75	0.5	0.251(3)	0.89(5)
O1	1	0.25	0	0.9993(2)	1.37(1)
O2	1	0.25	0.5	0.9982(2)	0.38(1)

O3	1	0.0111(1)	0	0.3056(1)	1.02(1)
O4	1	0.25	0.7684(1)	0.7080(1)	0.79(1)
O5	1	0.25	0.2495(1)	0.2799(1)	0.75(1)
O6	1	0.0039(1)	0.5	0.2664(1)	0.82(1)
O7	0.895(2)	0.25	0.5	0.5007(2)	0.43(2)
O8	0.129(1)	0.25	0	0.4956(12)	0.43(2)

Table 10. Co-O bond lengths (Å) calculated from the crystal structure model in Table 8 for $PrBaCo_2O_{5.52}$ sample. (a), (b), (c) represent the orientation of the Co-O bond, along a axis, b axis, and c axis, respectively. The subscript "L" and "R" stands for the two sides of Co ions. "Pyr" stands for pyramidal coordination, corresponding to the occupancy of "O4" in Table 8 and "Oct" for octahedral coordination, corresponding to the occupancy of "O3" in Table 8.

Metal	Co1(Pyr)	Co2(Oct)
O1(b)	1.898(1)	2.097(1)
O2(b)	1.898(1)	2.097(1)
O3(a)	1.991(1)	1.953(1)
O4(a)	1.991(1)	1.953(1)
O5(c)	1.922(3)	1.913(3)
O6		1.91(3)
Average(Co-O)	1.940	1.987

Table 11. Co-O bond lengths (Å) calculated from the crystal structure model in Table 9 for $PrBaCo_2O_{5.74}$ sample. (a), (b), (c) represent the orientation of the Co-O bond, along a axis, b axis, and c axis, respectively. The subscript "L" and "R" stands for the two sides of Co ions. "Pyr" stands for pyramidal coordination, corresponding to the occupancy of "O8" in Table 9 and "Oct" for octahedral coordination, corresponding to the occupancy of "O7" in Table 9.

Insulator	Co1(Pyr)	Co2(Pyr)	Co3(Oct)	Co4(Oct)
$O(b)_L$	1.982(1)	1.847(1)	1.987(1)	2.139(1)
$O(b)_R$	1.982(1)	1.847(1)	1.987(1)	2.139(1)
$O(a)_L$	1.919(1)	2.077(1)	1.927(1)	1.988(1)
$O(a)_R$	1.919(1)	2.077(1)	1.927(1)	1.988(1)
$O(c)_L$	1.888(3)	1.938(3)	1.929(3)	1.897(3)
$O(c)_R$			1.896(3)	1.89(3)
Average(Co-O)	1.9380	1.9572	1.9422	2.0068

4.1.5. XPS & XAS

At first, the possibility of charge ordering was investigated. Since the nominal valence for $PrBaCo_2O_{5.5}$ is 3+, charge ordering means the presence of Co^{2+} and Co^{4+} ions. Therefore, by looking for the Co^{2+} or Co^{4+} ions inside $PrBaCo_2O_{5.5}$ we can verify whether charge ordering is true or not. X-ray Photoemission Spectroscopy (XPS) is a very common technique to detect atom's velence state, so we measured the XPS spectra for $PrBaCo_2O_{5+x}$, x=0.18, 0.52, 0.74 respectively, as shown in Fig. 13(a). The spectra for $PrBaCo_2O_{5.18}$ and $PrBaCo_2O_{5.74}$ are set to be the reference as $PrBaCo_2O_{5.18}$ definitely contains Co^{2+} ions and $PrBaCo_2O_{5.74}$ has Co^{4+} ions in it. With comparison with these two spectra, it is possible to extract the charge information in $PrBaCo_2O_{5.52}$. However, just comparing the bind energy of "Co 2p 1/2" peak or "Co 2p 3/2" peak cannot give us any clue about the valence state of $PrBaCo_2O_{5.52}$ due to two problem. First is that the Co peaks are overlapped with the Ba peaks [Fig. 13(a)], causing a difficulty in precisely determining the bind energy for Co peaks. Even if the binding energy is known, it is still hard to distinguish the oxidation states for transition metals such as Fe, Mn and Co due to the tiny chemical shift between different oxidation states, which can be easily seen in the "B.E" columns of Fig. 13(c). In this case, the satellite peak, generally arising from the charge transfer effect [Fig. 13(b)], plays an important role in identifying the atom's valence state. Looking into the "S.S." columns of Fig. 13(c), we will find that distinct satellite positions for Co^{2+} and Co^{3+} ions. The satellite of Co^{2+} is located at about 6 eV higher than the main peak while that for Co^{3+} is over 9 eV away from the main peak. The spectra of Fig. 13(a) are all normalized to the same background level at about 770 eV for comparing the satellites. It can be seen that in $PrBaCo_2O_{5.18}$, composed of about 30% Co^{2+} and 70% Co^{3+}, a satellite peak appears at about 6.7 eV higher than the "Co 2p 3/2" peak, a featuring signal for Co^{2+}, while $PrBaCo_2O_{5.52}$ and $PrBaCo_2O_{5.74}$ do not have this satellite. The "Co 2p 3/2" peak position of $PrBaCo_2O_{5.18}$ is estimated by comparing the those of $PrBaCo_2O_{5.52}$ and $PrBaCo_2O_{5.74}$, as the peak position shift to higher bind energy by decreasing the oxygen content. Through this satellite, we can conclude that $PrBaCo_2O_{5.52}$, same as $PrBaCo_2O_{5.74}$, does not contain any Co^{2+} ions. Some supporting evidence can also be found in the Soft X-ray Absorption Spectra (XAS) in Fig. 13(d). For comparing the peak shape of "Co 2p 3/2" peaks, they were normalized to the same height. A

remarkable rise in the high-energy side can be observed in $PrBaCo_2O_{5.33}$ upon other compounds. $PrBaCo_2O_{5.33}$ consists of 20% $Co^{2+}$and 80% Co^{3+}, while the nominal valence state of Co ions in other compounds are over 3+, so this rise can be attribute to the contribution from Co^{2+} ions, denying the existence of Co^{2+} in $PrBaCo_2O_{5.52}$. Therefore, the charging ordering, reported in Ref. [24], should not occur in the insulator phase of $PrBaCo_2O_{5.52}$.

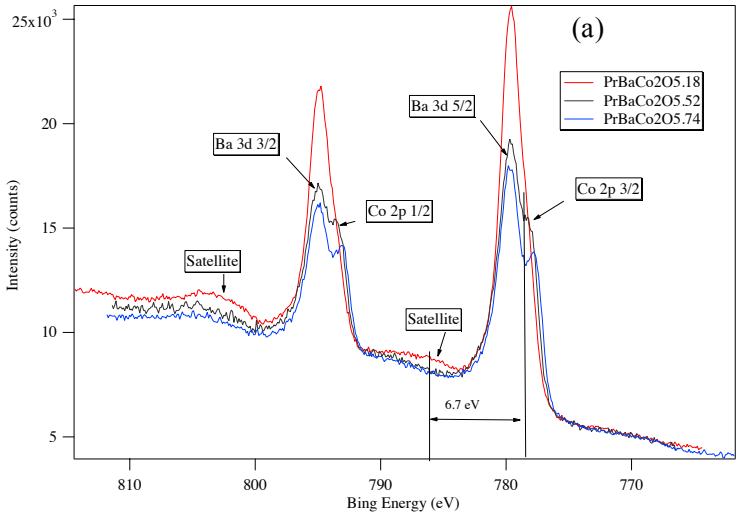

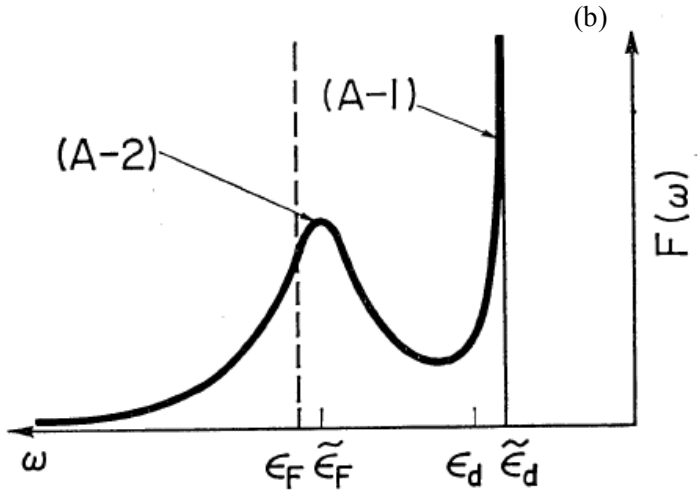

BINDING ENERGIES OF SPINELS AND RELATED COMPOUNDS

Compound	O.S.[a]	Co[b]	Metal $2p_{1/2}$ B.E.[c]	Metal $2p_{1/2}$ S.S.[d]	Metal $2p_{3/2}$ B.E.	Metal $2p_{3/2}$ S.S.	Methods of syn. ref.
Co_3O_4	Co^{2+}	T[e]	795.4	9.5	780.3		4
	Co^{III}	O[f]					
CoO	Co^{2+}	O	796.2	6.3	781.1	6.2	
$CoFe_2O_4$	Co^{2+}	O	705.7	6.2	779.9	6.2	5
$CoAl_2O_4$	Co^{2+}	T	796.7	6.3	781.0	5.0	4
$CoMn_2O_4$	Co^{2+}	T	796.3	6.5	780.2	5.6	6
$CoCr_2O_4$	Co^{2+}	T	796.3	6.2	780.4	5.3	6
$ZnCo_2O_4$	Co^{III}	O	795.7	9.4	780.6	9.4	7
$K_3Co(CN)_6$	Co^{III}	O	796.3	13.3	781.4		
Fe_3O_4	Fe^{2+}	O	724.4	7.9	710.6		
	Fe^{3+}	T+O					
$FeCr_2O_4$	Fe^{3+}	T	724.3	7.7	710.8		8
$CoFe_2O_4$	Fe^{3+}	T+O	724.4	8.1	711.0	5.1	5
α-Fe_2O_3	Fe^{3+}	O	725.0	8.1	711.4	8.6	
Mn_3O_4	Mn^{2+}	T	653.1	10.4	641.4		9
	Mn^{3+}	O					
MnO	Mn^{2+}	O	652.3	5.7	640.7	5.6	
$MnCr_2O_4$	Mn^{2+}	T	652.5	5.2	640.8	5.6	10
$CoMn_2O_4$	Mn^{3+}	O	653.2	10.0	641.7		6
α-Mn_2O_3	Mn^{3+}	O	653.5	10.0	641.9		
γ-Mn_2O_3	Mn^{3+}	T+O	653.4		641.7		
$CuMn_2O_4$			652.8	10.3	641.2		11

(c)

[a] oxidation state; [b] coordination type; [c] binding energy (eV); [d] satellite splitting (eV); [e] tetrahedral coordination; [f] octahedral coordination.

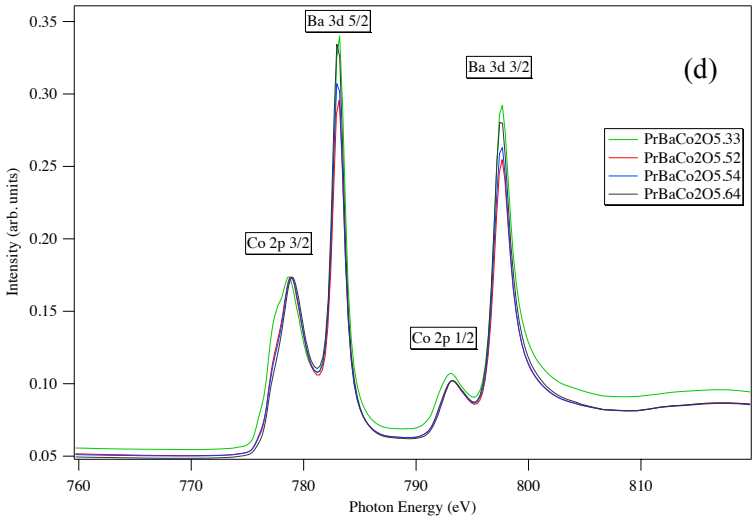

Fig. 13 (a) X-ray Photoemission Spectra (XPS) of $PrBaCo_2O_{5+x}$ (x=0.18, 0.52, 0.74) at room temperature (b) Schematical line shape of X-ray Photoemission Spectrum by considering the charge transfer effect [48] (c) Bind energies of some transition metal compounds [49] (d) Soft X-ray Absorption Spectra (XAS) of $PrBaCo_2O_{5+x}$ (x=0.33, 0.52, 0.54, 0.64) at room temperature.

On ruling out the possibility of charge ordering, we then concentrate on the spin state transition (SSI). Actually, the SSI has been observed in XAS spectra as shown in Fig. 14 (a), where the line shape of "Co 2p 3/2" peak at 379K differs from those at 322 K and 302 K, although the difference is quite small. Actually, the XAS spectra of $GdBaCo_2O_{5.5}$ [50] and $YBaCo_2O_{5.5}$ [35] exhibit analogous tiny difference between the insulator phase and the metal phase. Since the MIT occurs in the paramagnetic phase [Fig. 15 (a)], the average magnetic effective moment (μ_{eff}) can be extracted by Curie-Weiss law. The fitting was conducted on inverse susceptibility

curve [Fig. 9 (b)] the in the range of 280 – 320 K, and 360 – 400K , respectively, to get the effective moment below and above the T_{MI}. It is found that the μ_{eff} changes from 2.50 μ_B ($T < T_{MI}$) to 5.44 μ_B ($T < T_{MI}$). Because there are more than one non-equivalent Co sites and one Pr site in the unite cell, the specific for each Co site can not be obtained. But anyway, we can get to know the the spin state of Co^{3+} ions jumps up from insulator phase to metal phase. Also, it is noted that the fitting above T_{MI} gives a negetive curie temperature θ, indicating the antiferromagnetic interaction between Co^{3+} ions.

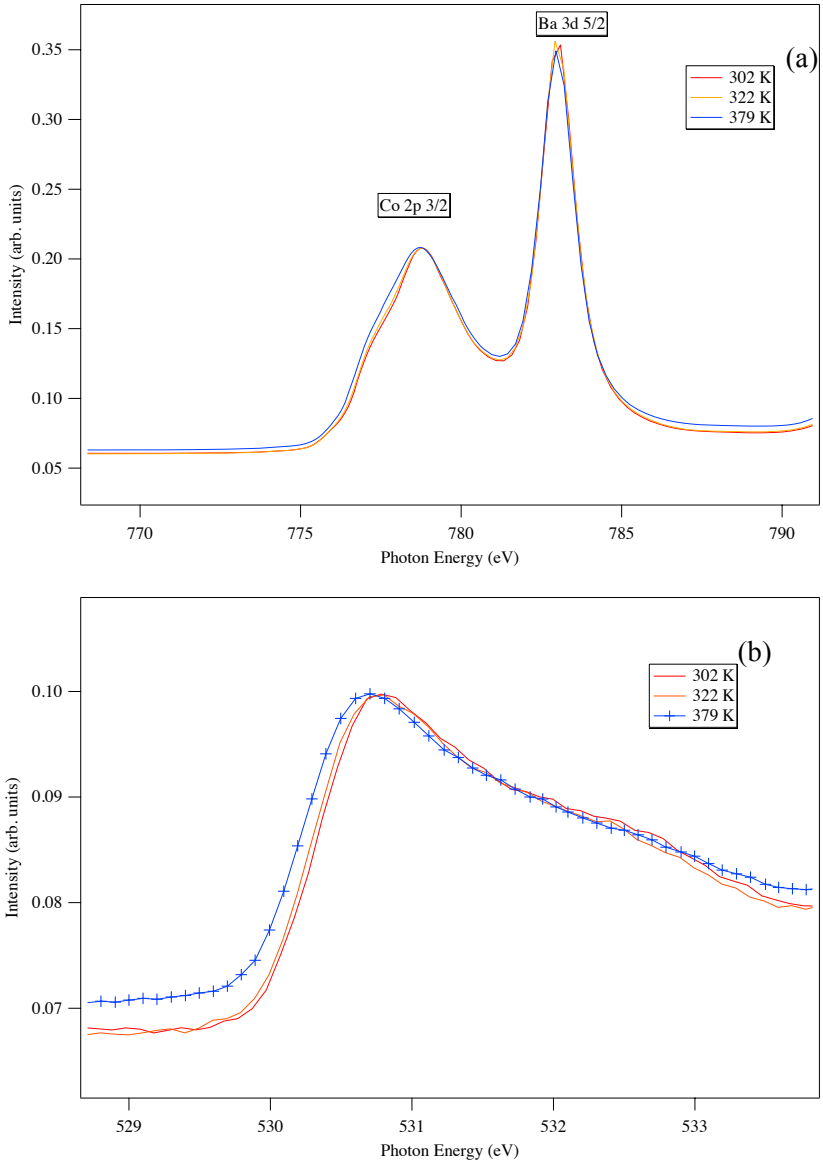

Fig. 14 (a) Co 2p 3/2 and Ba 3d 5/2 XAS spectra of $PrBaCo_2O_{5.52}$ at 302 K, 322 K, and 379 K. (b) O-K XAS spectra of $PrBaCo_2O_{5.52}$ at 302 K, 322 K, and 379 K.

4.1.6. Magnetic structure

As shown in Fig. 15(a), spontaneous magnetic moment emerges when cooling down from paramagnetic phase, achieves the maximum at about 225 K, and then vanishes abruptly. We believe that the magnetic structure at about 225 K may contain the information of spin state for each Co sites in insulator phase (T < 346 K). Thus, the low temperature neutron powder diffraction experiment was done in order to study the magnetic structure. Fig. 15(b) shows the intensity temperature dependence of some magnetic peaks. (1 1 1) peak first starts to rise from 255 K, and approachs maximum at about 230K, consistent with the magnetization. Another magnetic peak of (1 1 0.5) appears from about 235 K, exhibiting a transition to the second magnetic ordering phase. Hereafter we defined 255 K as T_C, 235 K as T_N, the phase between T_C and T_N as phase 1, the phase below T_N as phase 2, and the phase between T_C and T_{MI} as insulating PM phase. s we know, T_C is much high than the spin ordering temperature of Pr, which generally lower than 20K [51,52], so phase 1 only has Co ordering.

We believe that from PM phase to phase 1 it is the second order phase transition, in which only the moments of Co^{3+} ions turn to be ordered without changing the spin states, while from phase 1 to phase 2 the spin state transition of Co^{3+} ions occurs so as to make the antiferromagnetic ordering, which appears to be the first order phase transition. As a result, studying the magnetic structure of phase 1 would enable us to obtain the spin state of Co^{3+} ions in the insulating PM phase, which is crucible to understand the nature for MIT. Since phase 1 is of main interest, the long time neutron powder diffraction data was taken at both 225K and 237 K in order to study the magnetic structure in phase 1. As shown in Fig. 15(b) and Fig. 15(c), at 237 K is the pure phase 1, while at 225 K is the coexisting phase 1 and phase 2. AThe previous analysis on crystal sturecture allowed us to determine the propagation vector by indexing in the framework of Pmma ($2a_p \times 2a_p \times 2a_p$) and it is found to be (0, 0, 0). This result in turn indicates that the crystal structure does not change going from insulating PM phase to phase 1, which ensures us that the two phases share the same spin state. From the anisotropy in previous magnetization of untwinned $GdBaCo_2O_{5.5}$ crystal (Fig. 15(d)), we know that the all the magnetic moments of Co^{3+} ions lie along the a axis. Taking into account the antiferromagnetic interaction by the

negetive curie temperature θ, we assume an anti-parallel ordering of all the neighboring Co^{3+} ions along the a axis for the Rietveld refinement. Actually, this model was already justfied by the symmetry analysis and also muon spin relaxation measurement [26,27].

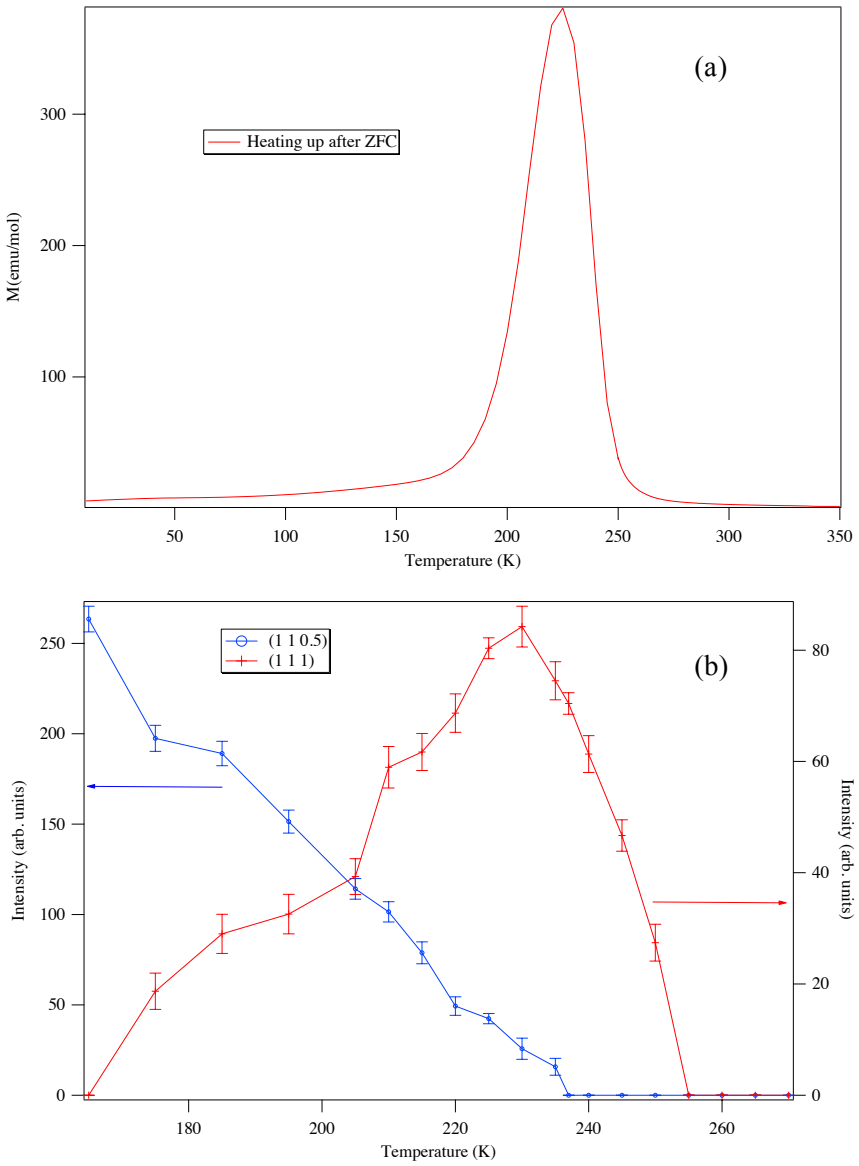

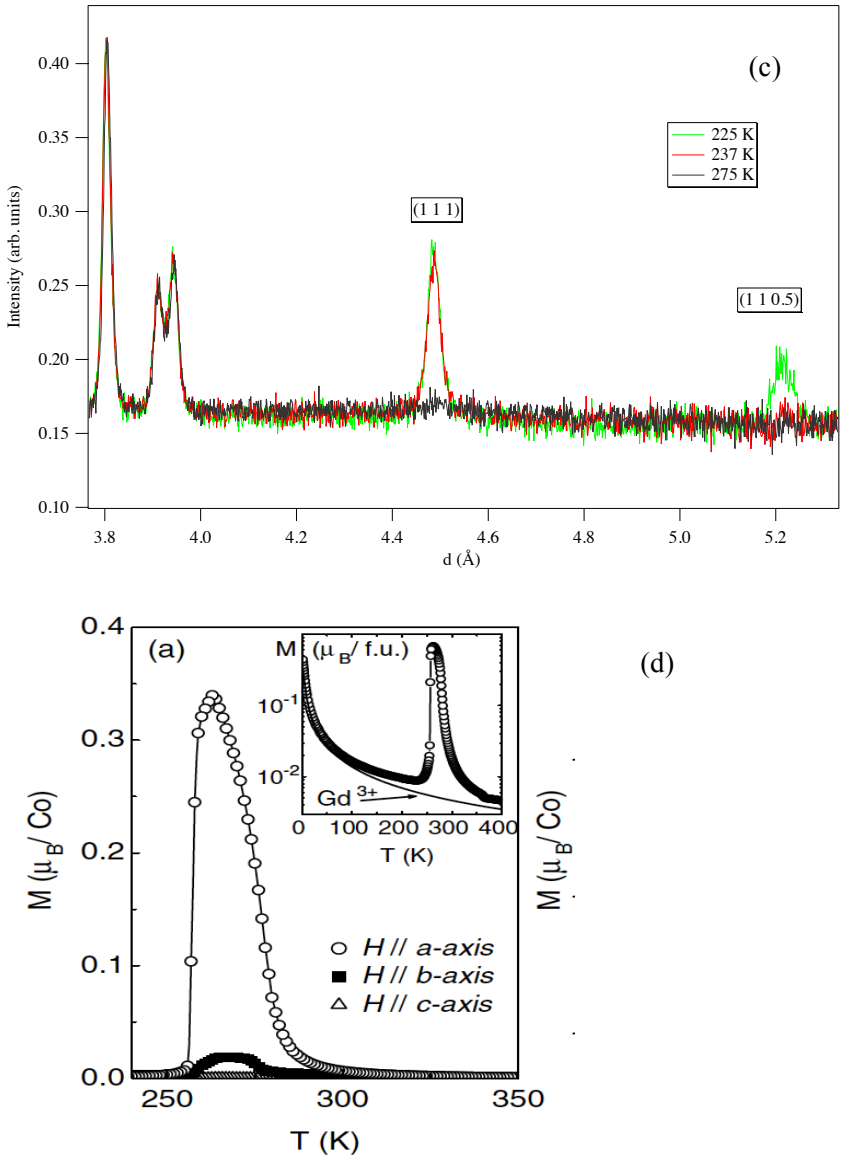

Fig. 15 (a) Temperature dependence of magnetization for $PrBaCo_2O_{5.52}$ measured in the field 100 Oe after zero fied cooling (ZFC) (b) Intensity temperature dependence of reflections (1,1,1) and (1,1,0.5) from neutron powder diffraction on $PrBaCo_2O_{5.52}$. Indices are given for the unit cell ($2a_p \times 2a_p \times 2a_p$) (c) Part of neutron diffraction pattern at 225K, 237K and 275K. Indices are given for the unit cell ($2a_p \times 2a_p \times 2a_p$). (d) Magnetization of an untwinned $GdBaCo_2O_{5.5}$ single crystal measured in H = 0.1 T applied along one of the crystal axes (contribution of Gd^{3+} ions is subtracted). Inset: raw M(T) data for H || a, where the solid line shows the Curie-Weiss contribution of Gd^{3+} ions (μ_{eff} = 7:94 μ_B; θ = 0 K) [22].

The refinement strategy is as follows: First, the data at 275 K (paramagnetic phase) was refined to get the crystal structure. By comparison of diffraction pattern at short d range, where the magnetic form factor shown in Fig. 16(a) are relatively small, we found that the intensity for

each index almost maintains to be the same at 275 K, 237 K and 225 K as shown in Fig. 16(b), indicating that the atomic positions do not change much at this temperature range. So when analyzing the data at 237K and 225K, the crystal structure at 275 K was adopted as the initial model with all the atomic positions fixed, only refining the lattice constant. The magnetic moments of each Co site were refined based on this crystal structure. The final magnetic structure is shown in Fig. 16(c) and the magnitudes of magnetic moments are listed in Table 12. Co3(Oct) has no magnetic moments with its error bar, obviously in the non-magnetic LS state. As for other Co sites, the moments exhibit a large deviation from the saturate moments, which are 2 μ_B for IS state and 4 μ_B for HS state, respectively. Below 230 K the magnetization abruptly drops [Fig. 15(a)] because of the phase transition to phase 2, which does not mean that the magnetic moments in phase 1 achieve saturation at 230 K. It is highly possible that 230 K still resides in the crytical region, where a large thermal fluctuation for the magnetic moments occurs. Actually, the thermal fluctuation clearly manifests itself in the temperature dependence of the magnitude of magnetic moments in Fig. 16(d). Therefore, considering the large difference in the absolute value of the moments, we assign Co1(Pyr) and Co4(Oct) in IS state, Co2(Pyr) in HS state, listed in Table 12.

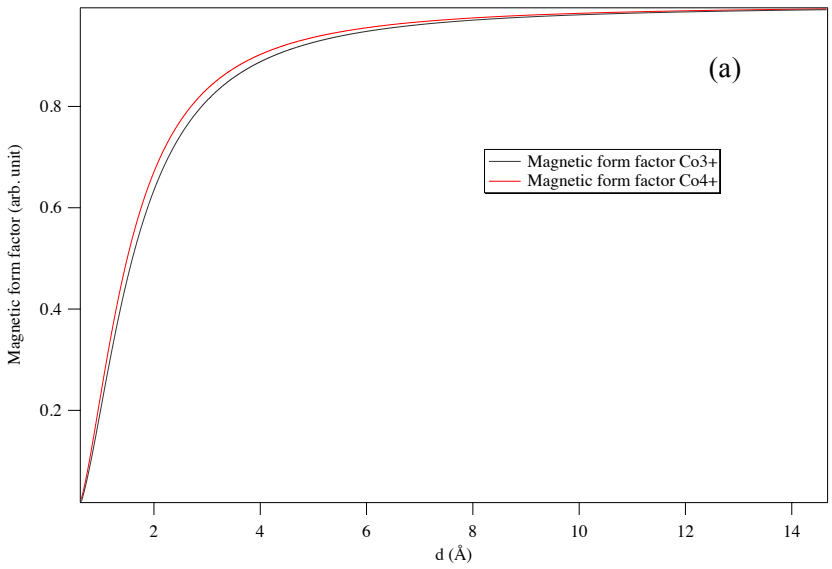

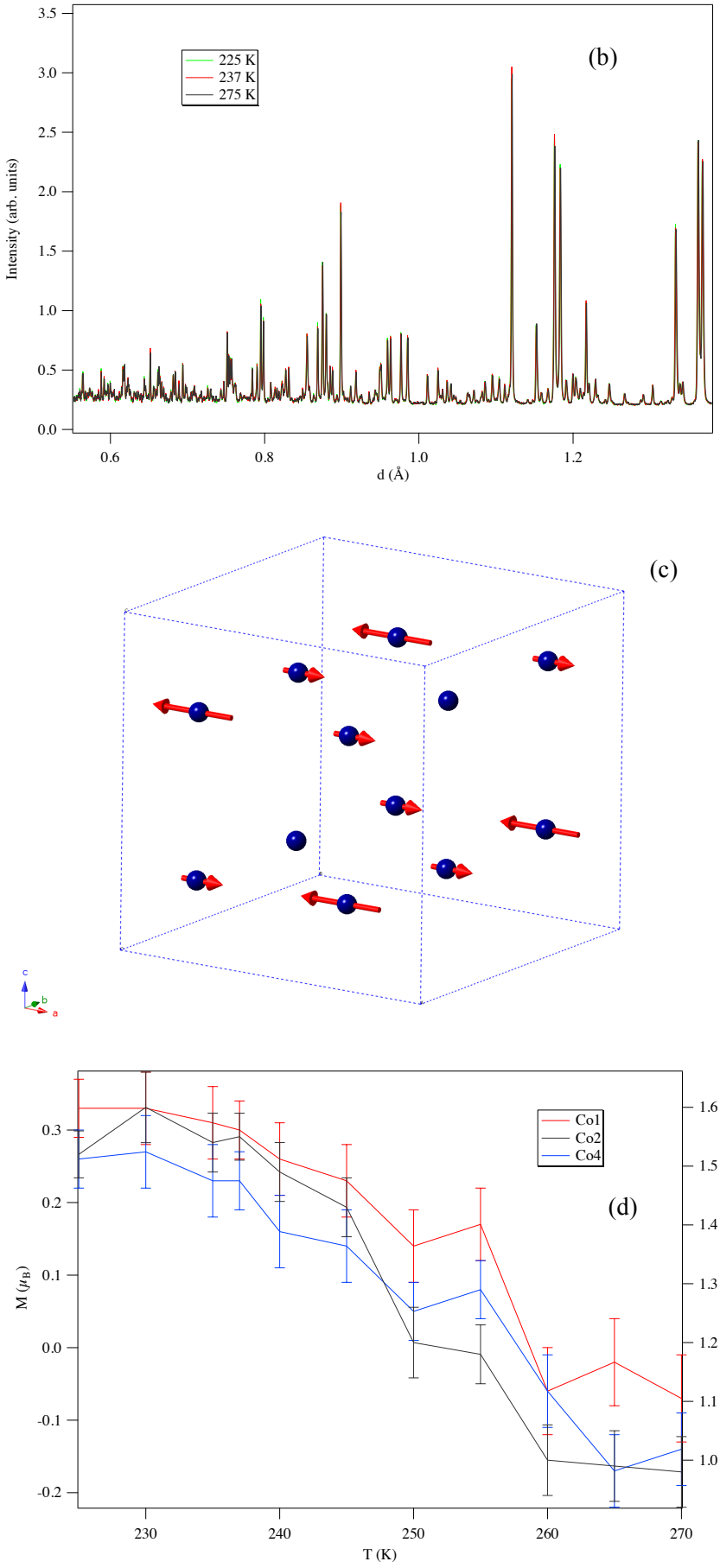

Fig. 16 (a) d-spacing dependence of magnetic form factor for Co^{3+} and Co^{4+}, respectively. (b) Part of neutron diffraction pattern at 225K, 237K and 275K at short d range. (c) A sketch of the magnetic structure of

$PrBaCo_2O_{5.52}$, in the framework of the single crystal unit cell with propagation vector (0 0 0), only Co ions are shown, the arrow on which denotes the moment of the Co^{3+} ions. Co ions without arrows exhibit zero magnetic moment (LS state). (d) Temperature dependence of the magnitude of magnetic moments for Co1 (left axis), Co2 (right axis), and Co4 (left axis).

With the knowledge of the fact that the spin state of Co^{3+} ions jumps up from insulator phase to metal phase, the spin state of Co_{pyr} and Co_{oct} in metal phase are expected to be in HS state and IS state, respectively. The origin for the structure phase transition from Pmmm ($a_p \times 2a_p \times 2a_p$) to Pmma ($2a_p \times 2a_p \times 2a_p$) lies in that half of HS Co_{pyr} ions switch into IS state and half of IS Co_{oct} ions into LS state.

Table 12. Magnetic moment values for each Co site in the frame work of Pmma ($2a_p \times 2a_p \times 2a_p$) with propagation vector (0, 0, 0). R_{wp} = 7.85 % for data at 237K, 7.64 % at 225K.

Phase 1	Co1(Pyr)	Co2(Pyr)	Co3(Oct)	Co4(Oct)
M(μ_B) at 237K	0.30(4)	-1.55(4)	0.01(4)	0.23(4)
M(μ_B) at 225K	0.33(4)	-1.52(4)	0.00(4)	0.26(4)
Spin state	IS	HS	LS	IS

4.1.7. Mechanism for MIT

.

Now, the origin of the structure phase transition from Pmma ($2a_p \times 2a_p \times 2a_p$) to Pmmm ($a_p \times 2a_p \times 2a_p$) coupling with the MIT is temperature induced SST in both pyramids and octhedra, where half IS octahedra switch into LS state, and half IS pyramid into HS state, for the fact that μ_{eff} gets larger when entering the metal state, as schematically shown in Fig. 17 (a) and Fig. 17 (b).

The mechanism for the MIT can lies in the LS Co3 in insulator phase as shown in Fig. 17 (a). The a glide plane perpendicular to c axis helps to create a 3-dimensional network of LS Co ions, as shown in Fig. 17 (c). A possible senario is like this: changing from IS state to LS state makes

Co3 lose the only e_g electron, leaving the empty e_g orbital. Since the hybridization with the O 2p orbitals is larger for e_g than for t_{2g}, losing the only e_g electron greatly the reduces the hopping parameters, in other words, increases the activation energy, resulting in a sudden drop of conductivity. This activation energy increase will open a larger gap between conduction band and valence band, which has been observed in the O k-edge XAS spectra [Fig. 14 (b)], the structures of which are due to transitions from the O 1s core level to the O 2p orbitals that are mixed into the unoccupied Co 3d t_{2g} and e_g states [53,54]. Thus, the O k-edge XAS spectra reflects the the density of states of the unccupied Co 3d orbital, i.e., the bottom of conduction band. As we can see, the threshold of spectra in the insulaor phase (at 302K, and 322K) shift to a higher energy side, indicating the increase of the band gap.

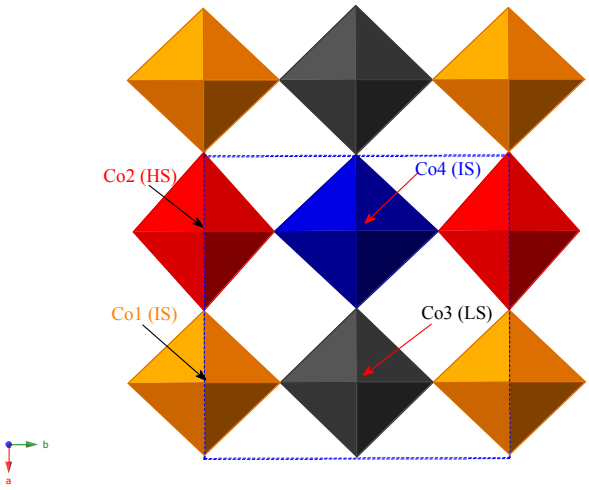

(c)

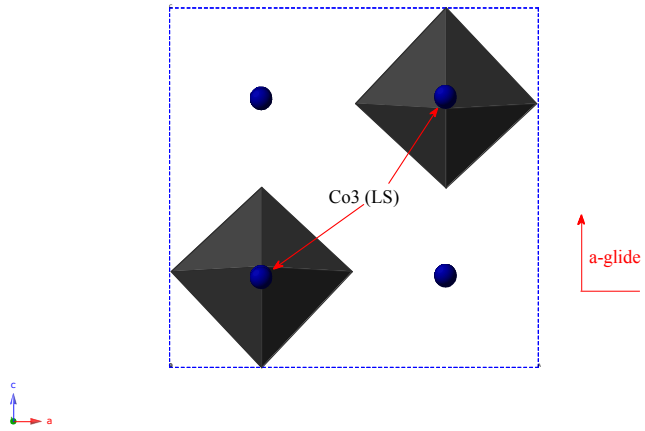

Fig. 17 (a) Schematic drawing for Co coordinations of $PrBaCo_2O_{5.5}$ (ab plane view) in insulator phase. Red polyhedrons stand for pyramids, black for octahedra. Blue dash line denotes the ($2a_p \times 2a_p \times 2a_p$) unit cell. (b) Schematic drawing for Co coordinations of $PrBaCo_2O_{5.5}$ (ab plane view) in metal phase. Red polyhedrons stand for pyramids, black for octahedra. Blue dash line denotes the ($a_p \times 2a_p \times 2a_p$) unit cell. (c) Schematic drawing for LS Co3 coordinations (black polyhedrons) of $PrBaCo_2O_{5.5}$ (ac plane view) in insulator phase. Blue dash line denotes the ($2a_p \times 2a_p \times 2a_p$) unit cell.

4.2. Hole doping induced Metal-Insulator Transition (MIT) for $PrBaCo_2O_{5.5+\delta}$

4.2.1. Resistivity

As shown in Fig. 18(a) and Fig. 18(b), the resistivity at room temperature drops abruptly, over one order of magnitude, by slightly increasing the oxygen content from $PrBaCo_2O_{5.52}$, in other words, by doping holes into the parent $PrBaCo_2O_{5.5}$. At high temperature range, the resistivity of $PrBaCo_2O_{5.64}$ is lower than that of $PrBaCo_2O_{5.74}$, and it looks to be some kink. This may be due to the fact that powder samples in pellet form were used for the resistivity measurement so that the grain-to-grain resistance can vary from sample to sample. Actually, the result from single crystal $GdBaCo_2O_{5.5+\delta}$ clearly shows a monotonic oxygen content dependence of the resistivity without any kink [19]. As a result, this sudden change in resistivity can be defined as the hole doping induced MIT. The transition doping level resides in oxygen content increment x = 0.10, i.e., 10% holes. Hereafter, we define $PrBaCo_2O_{5.5+\delta}$ with $\delta < 0.10$ at room temperature as insulating phase and $PrBaCo_2O_{5.5+\delta}$ with $\delta > 0.10$ at room temperature as metal phase although throughout the whole range of hole doping level in Fig. 18(a), $PrBaCo_2O_{5.5+\delta}$ present the semiconducting behavior.

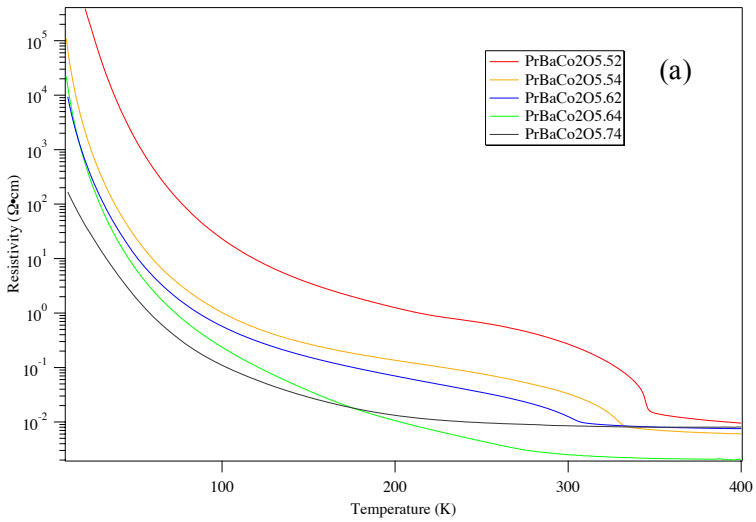

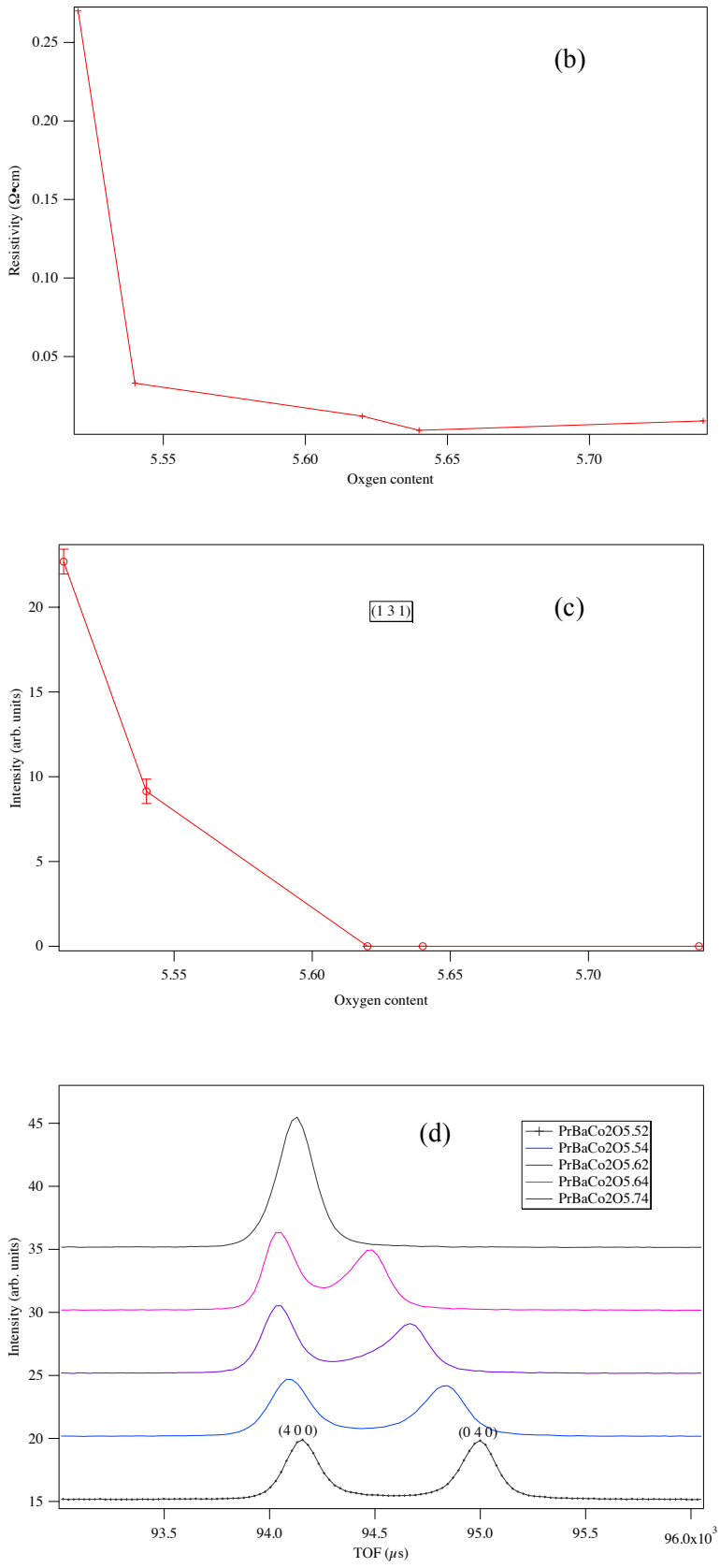

Fig. 18 (a) Temperature dependence of resistivity for $PrBaCo_2O_{5.5+\delta}$ (b) Oxygen content dependence of resistivity for $PrBaCo_2O_{5.5+}$ measured at room temperature (c) Oxygen content dependence of integrated intensity for (1 3 1) for $PrBaCo_2O_{5.5+\delta}$ measured by SuperHRPD at room temperature. The index are

given for the unit cell ($2a_p \times 2a_p \times 2a_p$) (d) Oxygen content dependence of diffraction patterns for (4 0 0) and (0 4 0) for $PrBaCo_2O_{5.5+\delta}$ measured by SuperHRPD at room temperature. The indices are given for the unit cell ($2a_p \times 2a_p \times 2a_p$)

4.2.2. Crystal structure

Neutron powder diffraction experiment was performed to study the structure transformation coupling with this MIT. It can be seen in Fig. 18(c) that the featuring peak (1 3 1) for the crystal structure of Pmma ($2a_p \times 2a_p \times 2a_p$) vanishes when entering the metal phase (x = 0.12), indicating a transition to the structure with ($a_p \times 2a_p \times 2a_p$) or ($a_p \times a_p \times 2a_p$) unit cell. ($a_p \times 2a_p \times 2a_p$) unit cell corresponds to the oxygen ordering (Inside Pr layer) model with orthorhombic space group Pmmm while ($a_p \times a_p \times 2a_p$) corresponds to the oxygen disordering (Inside Pr layer) model with tetragonal space group P 4/mmm. Looking into Fig. 18(d), the splitting between (4 0 0) and (0 4 0) peaks maintains until x = 0.14, a clear evidence for the orthorhombic structure. As a result, it can be concluded that hole doping induced MIT is coupling with the structure phase transition from Pmmm ($a_p \times 2a_p \times 2a_p$) to Pmma ($2a_p \times 2a_p \times 2a_p$).

When the oxygen content goes to 5.74, it seems that the two peaks merge into a single peak, possibly transform to the tetragonal structure. By Rietveld refinement with both models, we got the criteria R_{wp} of 8.43% for P4/mmm ($a_p \times a_p \times 2a_p$) and 6.83% for Pmmm ($a_p \times 2a_p \times 2a_p$). Although the fit goodness of Pmmm is better than that of P4/mmm, it is obvious that such a small difference cannot allow us to distinguish the two models.

By looking carefully into the diffraction pattern, we found some peak at 2.24 Å of d spacing (referred as peak A hereafter) keeps the single the index in both structure models, while another peak at 1.95 Å (referred as peak B hereafter) has two indices in Pmmm ($a_p \times 2a_p \times 2a_p$) and one index in P4/mmm ($a_p \times a_p \times 2a_p$) [Fig. 19(a)]. Since the FWHM/d's are generally a constant for all the single peaks, by comparing the FWHM/d of these two peaks, it would be possible to know whether the peak B is a single peak or overlapped double peaks. The FWHM/d's for peak A and B are 0.17% and 0.25%, respectively, illustrating that peak B is much broader than peak

A. So peak B is proved to be overlapped double peaks, justifying the orthorhombic crystal system for $PrBaCo_2O_{5.74}$. Actually, as shown in Fig. 19(b), super lattice peaks (0 1/2 3) and (1 1/2 1) indexed by ($a_p \times a_p \times 2a_p$) unit cell were clearly observed in the diffraction pattern, confirming the ($a_p \times 2a_p \times 2a_p$) unit cell.

The same evidence was found by electron diffraction pattern as well, as shown in [Fig. 19(c)], where super lattice spot (0 1/2 1) (marked by rectangle) indexed by ($a_p \times 2a_p \times 2a_p$) unit cell exists. Actually, another combination with (1/2 1/2 0) for rectangle, (0 0 2) for circle, can also be assigned to the spots if just considering the d-spacing. However, the diffraction pattern in Fig. 19(d) eliminated this possibility as only (1 1 0) reflection can be seen in the pattern.

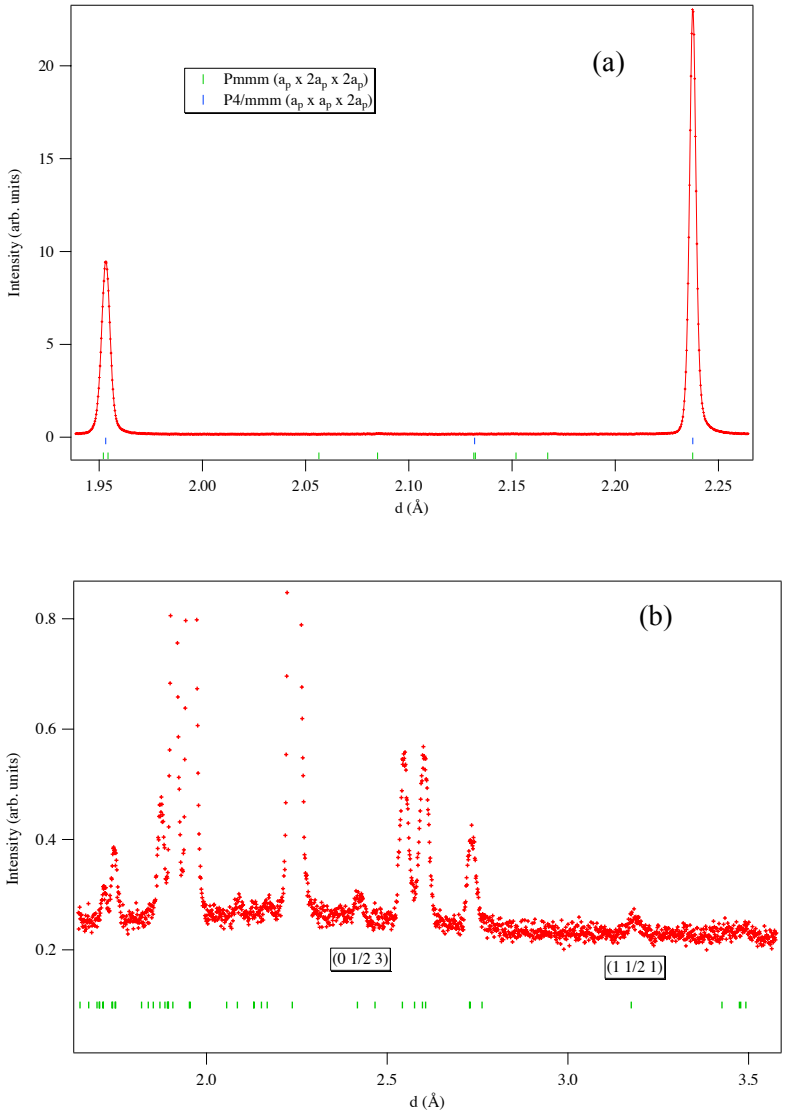

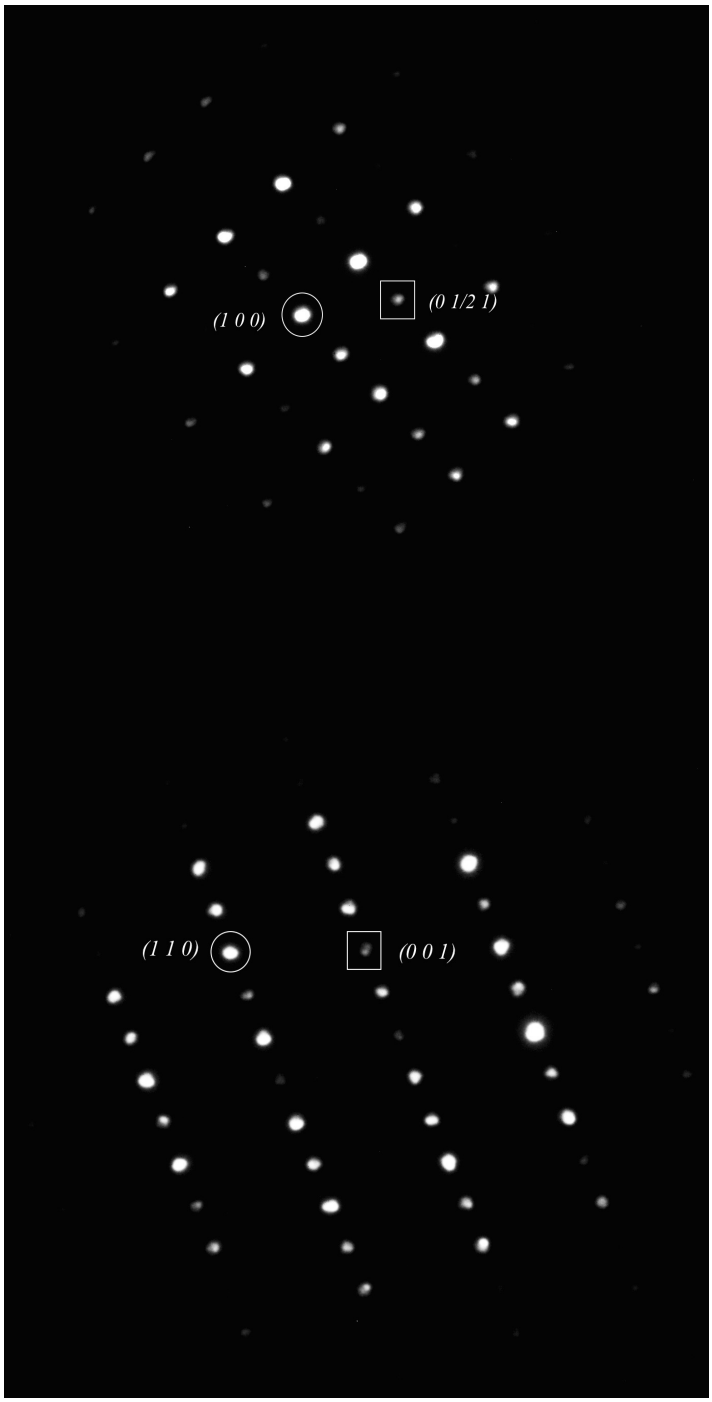

Fig. 19 (a) Part of the neutron diffraction pattern for $PrBaCo_2O_{5.74}$ measured at room temperature, The indices are given by Pmmm ($a_p \times a_p \times 2a_p$) and P4/mmm ($a_p \times a_p \times 2a_p$), respectively. (b) Supper lattice peaks (0 1/2 3) and (1 1/2 1) indexed (green bars) by unite cell ($a_p \times a_p \times 2a_p$) (c, d) Electron diffraction pattern of $PrBaCo_2O_{5.74}$ at room temperature indexed by the $a_p \times a_p \times 2a_p$ unit cell. Multiple scattering was checked during the measurement. In (c), the rectangle marks (0 1/2 1) reflection and the circle marks (1 0 0) reflection. In (d), the rectangle marks (0 0 1) reflection and the circle marks (1 1 0) reflection.

The crystal structure parameters determined by Rietveld refinement based on this oxygen ordering model are listed in Table 13 and the resultant Co – O bond lengths are shown Table 14. It illustrates nonequivalent occupancies for the two oxygen sites in Pr layer and also the Co–O bond lengths along a and b axes have significant differences from each other, further verifying the orthorhombic oxygen ordering model. Therefore, we demonstrate that when entering the metal phase, not just for $PrBaCo_2O_{5.62}$, but even for $PrBaCo_2O_{5.74}$, the orthorhombic Pmmm ($a_p \times 2a_p \times 2a_p$) oxygen ordering model, instead of the tetragonal P4/mmm ($a_p \times a_p \times 2a_p$) oxygen disordering model reported in Ref. [19,37,38], is the best to describe its crystal structure.

Table 13. Crystal structure parameters, including occupancy, atomic coordinates, and displacement parameters, determined for $PrBaCo_2O_{5.74}$ sample at room temperature from the neutron powder diffraction data, using orthorhombic space group Pmmm ($a_p \times 2a_p \times 2a_p$). The lattice constant and the criteria of the Rietveld refinement quality are: a = 3.89832(1) Å, b = 7.90892(2) Å, c = 7.64649(2) Å; Rwp = 6.83%.

Atom	Occupancy	x	y	z	100U
Ba	1	0.5	0.2507(1)	0	0.09(2)
Pr	1	0.5	0.2654(1)	0.5	0.56(3)
Co1	1	0	0	0.2524(2)	0.41(4)
Co2	1	0	0.5	0.2494(2)	0.49(3)
O1	1	0	0	0	1.25(3)
O2	1	0	0.5	0	0.84(3)
O3	0.813(5)	0	0.5	0.5	0.45(4)
O4	0.652(6)	0	0	0.5	1.11(4)
O5	1	0.5	0	0.2874(2)	1.39(2)
O6	1	0.5	0.5	0.2715(2)	1.18(2)
O11	1	0	0.2484(1)	0.2763(1)	1.45(2)

Table 14. Co-O bond lengths (Å) calculated from the crystal structure model in Table 13 for $PrBaCo_2O_{5.74}$ sample. (a), (b), (c) represent the orientation of the Co-O bond, along a axis, b axis, and c axis, respectively. The subscript “L” and “R” stands for the two sides of Co ions.

Metal	Co1	Co2
$O(b)_L$	1.949(1)	1.975(1)

$O(b)_R$	1.949(1)	1.975(1)
$O(a)_L$	1.973(2)	1.962(2)
$O(a)_R$	1.973(2)	1.962(2)
$O(c)_L$	1.927(5)	1.904(4)
$O(c)_R$	1.89(4)	1.913(5)
Occpancy ($O(c)_R$)	0.652(6)	0.813(5)
Average(Co-O)	1.9435	1.9485

4.2.3. Magnetic structure

As shown in Fig. 20(a) and Fig. 20(a), the magnetization of $PrBaCo_2O_{5.74}$ behaves in the way analogous to that of $PrBaCo_2O_{5.52}$, with the maximum just shifting to a lower temperature, at about 85 K. The hysteresis in the isothermal magnetization of $PrBaCo_2O_{5.74}$ at 100 K in Fig. 20(b) exhibits clear evidence of the spontaneous magnetic moment, which comes either from ferromagnetic ordering or ferrimagnetic ordering. On cooling below 85 K, a sudden decrease of the magnetization indicates possibly occurance of a SST or magnetic structrue phase transition. Also the evidence of magnetic moment ordering was observed in the low temperature neutron powder diffracton pattern in terms of apearance of some magnetic peaks. The intensity temperature dependence of one of them is shown in Fig. 20(c), which is coincident with the magnetization curve in Fig. 20(a). The magnetic peak appears from about 150 K (set as T_c) hereafter, and it rises to the maximum at about 80 K (set as T_{max}), followed by the decreasing of the intensity until the best temperature measured (5K). As shown in Fig. 14(a), above T_c it turns out to be a single paramagnetic phase without any SST, which is different from that of $PrBaCo_2O_{5.52}$. Another discrepancy lies in that upon cooling down across T_{max}, no additional peak was observed in the diffraction pattern of $PrBaCo_2O_{5.74}$, while $PrBaCo_2O_{5.52}$ enters from phase 1 to phase 2 coupling with appearance of some new peaks. So at this moment, it is hard to say whether there is a new phase below T_{max} for $PrBaCo_2O_{5.74}$. However, analogous to $PrBaCo_2O_{5.52}$, we also believe that the phase transition at T_c present to be second order so that by analysis of the magnetic structure between T_c and T_{max}, defined as phase FM, the spin state of Co^{3+} ions in the paramagnetic phase will be clarified.

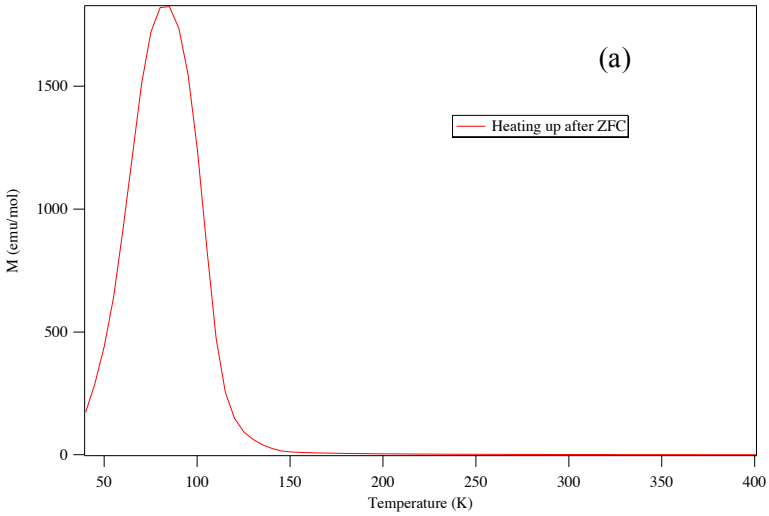
(a)
Heating up after ZFC
M (emu/mol)
Temperature (K)
0
500
1000
1500
50
100
150
200
250
300
350
400

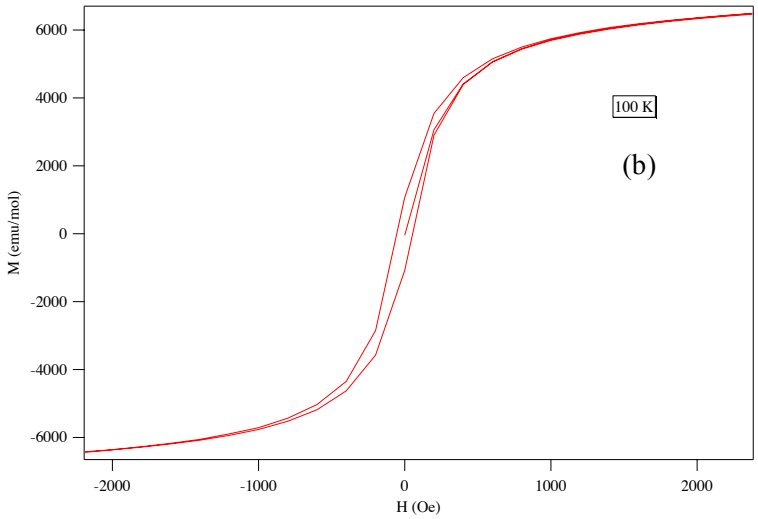
100 K
(b)
M (emu/mol)
H (Oe)
6000
4000
2000
0
-2000
-4000
-6000
-2000
-1000
0
1000
2000

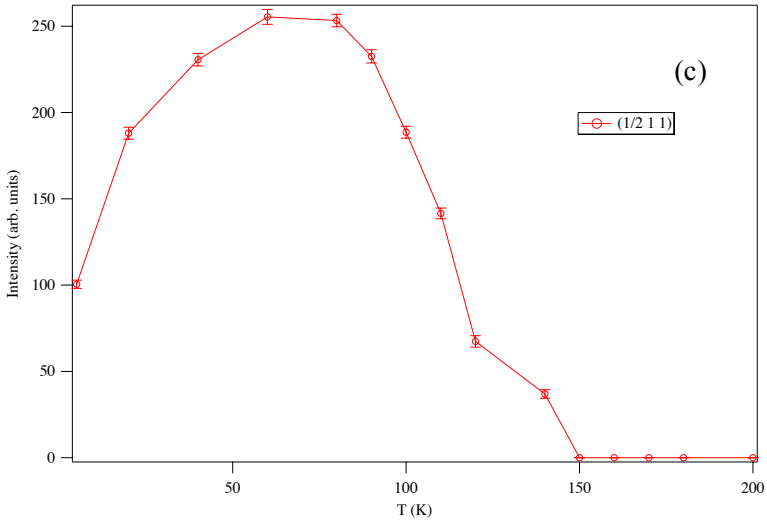
(c)
(1/2 1 1)
Intensity (arb. units)
T (K)
0
50
100
150
200
250
50
100
150
200

Fig. 20 (a) Temperature dependence of magnetization for $PrBaCo_2O_{5.74}$ measured in the field 100 Oe after zero fied cooling (ZFC). (b) Isothermal magnetization for $PrBaCo_2O_{5.74}$ measured at 100 K. (c) Intensity temperature dependence of magnetic reflection (1/2,1,1) indexed by unit cell ($a_p \times 2a_p \times 2a_p$) from neutron powder diffraction on $PrBaCo_2O_{5.74}$.

On the basis of the crystal structrue anaylsis above, the propagation vector for phase FM was determined to be (1/2, 0, 0) in the framework of Pmmm ($a_p \times 2a_p \times 2a_p$), signaling a ferromagnetic magnetic structure. By symmetry analysis, it is found that the basis vector for the magnetic moment cannot align in any direction other than the axial direction, a or b or c axis and six possible magnetic structures may be possible in the framework of Pmmm ($a_p \times 2a_p \times 2a_p$), as shown in Fig. 21. It is easy to see the structure in Fig. 21(a - c) contains some ferromagnetic ordering either along a or b or c, while pure ferromagnetic structures are present in Fig. 21(d - f). Thus, the canted G-type antiferromagnetic structure in the framework of tetragonal crystal structure in Ref. [37] can be eliminated.

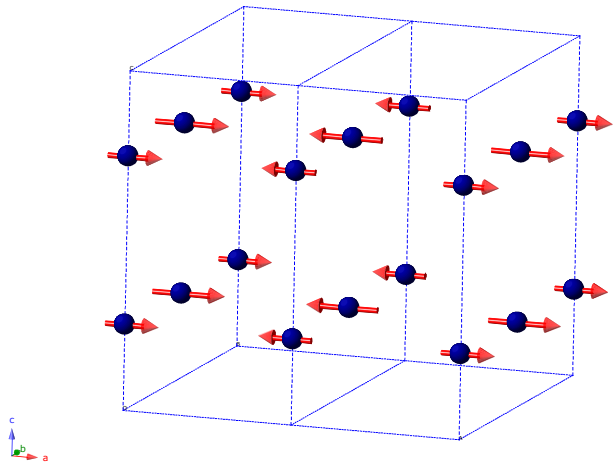

(a)

(b)

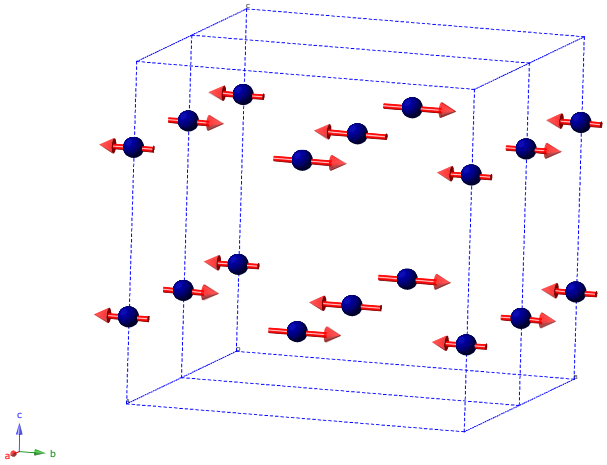

(c)

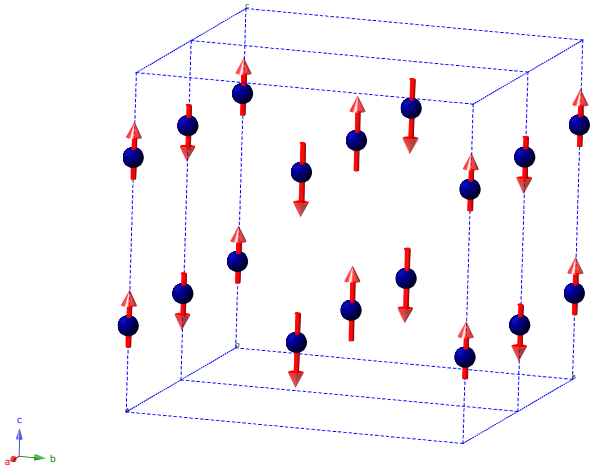

(d)

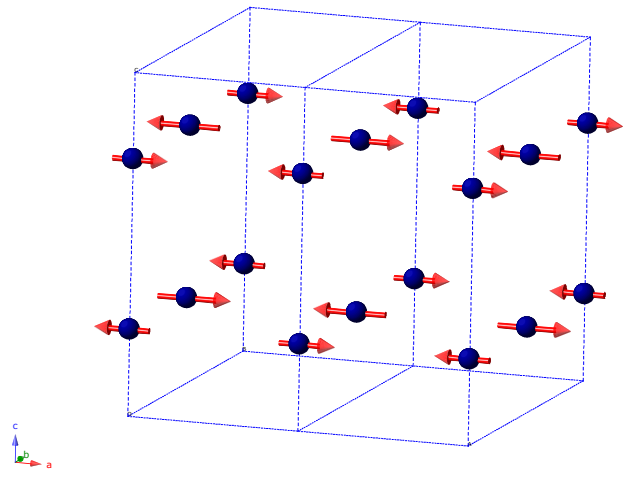

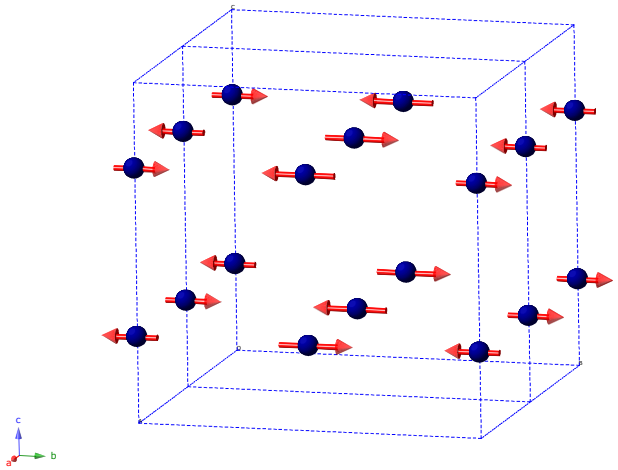

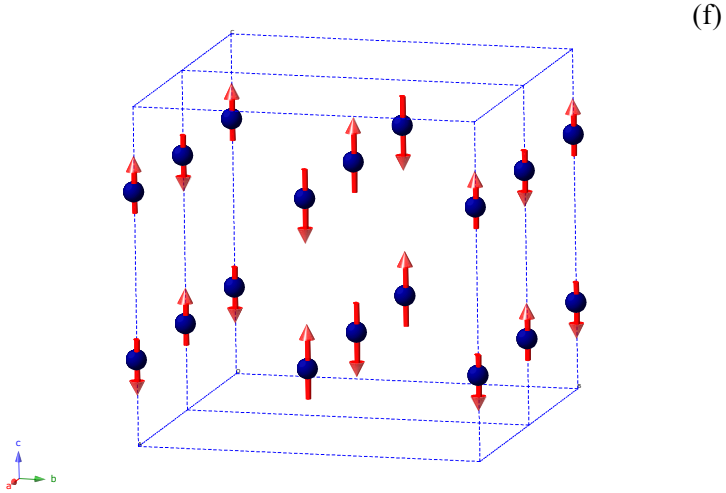

Fig. 21 The possible magnetic structures of $PrBaCo_2O_{5.52}$, in the framework of the double crystal unit cells with propagation vector (1/2 0 0), only Co ions are shown, the arrow on which denotes the moment of the Co^{3+} ions. Magenetic moments are along a axis in (a, d), along a axis in (b, e), and along c axis in (c, f).

The Rietveld refinement strategy is almost the same as that for $PrBaCo_2O_{5.52}$. But should be noted that $PrBaCo_2O_{5.74}$ is not composed of pure Co^{3+} ions, and it actually contains about 25% Co^{4+} ions and 75% Co^{3+} ions. Generally, Co^{3+} ions and Co^{4+} ions should be separated since the magnetic form factors for both are different in principle. However, the calculation as shown in Fig. 16(a) demonstrates that they are so close that it allows an approximation of adopting the identical magnetic form factor for them. In this way it is not necessary to divide Co^{3+} ions and Co^{4+} ions into two groups anymore, and consequently the number refined parameters are reduced, improving the reliability of the refinement.

It is found that the calculated magnetic structure factor for magnetic reflection (1/2,1,1) indexed by unit cell ($a_p \times 2a_p \times 2a_p$) is zero, as shown in Fig. 22(a), using the magnetic structures with ferromagnetic components in Fig. 21(a - c), thus eliminating the three models. For structures in Fig. 21(d - f), the only difference are just along a or b or c axis, so all of them can give good fittings in the Rietveld refinement. Therefore, conclusion can be drawn that $PrBaCo_2O_{5.74}$ owns the ferrimagnetic structure.

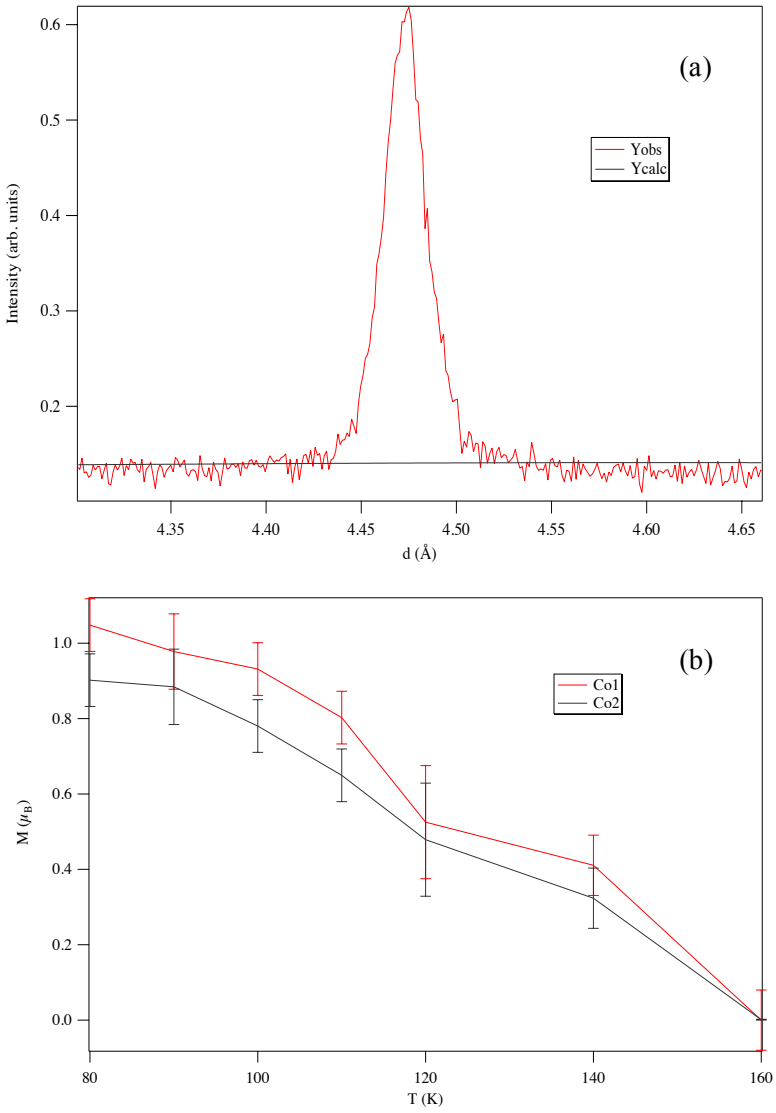

(c)

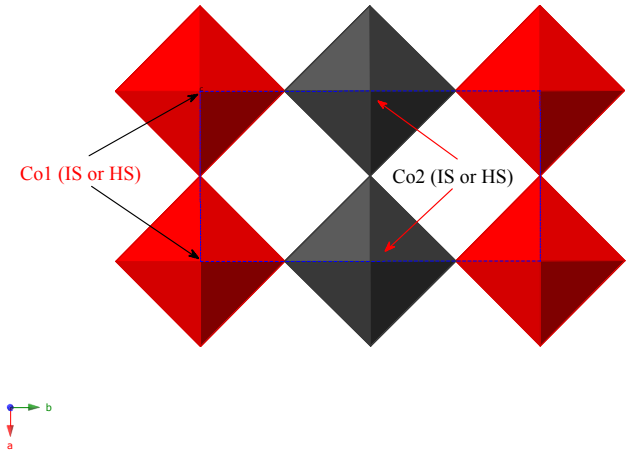

Fig. 22 (a) Observed intensity (Yobs) and calculated intensity (Ycalc) of magnetic reflection (1/2,1,1) indexed by unit cell ($a_p \times 2a_p \times 2a_p$) in Rietveld refinement from neutron powder diffraction data on $PrBaCo_2O_{5.74}$ at 80 K. (b) Temperature dependence of the magnitude of magnetic moments for Co1 and Co2. (c) Schematic drawing for Co coordinations of $PrBaCo_2O_{5.74}$ (ab plane view) in metal phase. Red polyhedrons stand for pyramids, black for octahedra. Blue dash line denotes the ($a_p \times 2a_p \times 2a_p$) unit cell.

Since $PrBaCo_2O_{5.52}$ exhibits a large anisotropy of magnetization along a axis, we assume the magnetic moments of $PrBaCo_2O_{5.74}$ lie along a axis as well. The final ferrimagnetic structure is shown in Fig. 21(d) and the magnitudes of magnetic moments at 80 K are listed in Table 12. Same as $PrBaCo_2O_{5.52}$, the magnetic moments of $PrBaCo_2O_{5.74}$ demonstrates a large thermal fluctuation as is shown in Fig. 22(b). The magnitude of magnetic moment is an average value contributed by both Co^{3+} ions and Co^{4+} ions. Co^{4+} ion is always in the LS state with only one unpaired electron, so magnetic moment at maximum is 1 μ_B if thermal fluctuation is not taken into account. 25% of Co^{4+} ions make at most 0.25 μ_B to M(μ_B) at 80 K for either Co1 or Co2. As a result, a major component of M(μ_B) for Co1 and Co2 comes from the Co^{3+} ions, which, in other words, illustrate that Co1 and Co2 are not in the nonmagnetic LS state. As was proved in $PrBaCo_2O_{5.52}$, half of the octahedral Co^{3+} ions are in LS state in insulating paramagnetic phase. Here we show that hole doping introduces the SST from LS state to either IS state or HS state. Because of this hole doping induced SST, the structure phase transition from Pmma ($2a_p \times 2a_p \times 2a_p$) [Fig. 17(a)] to Pmmm ($a_p \times 2a_p \times 2a_p$) [Fig. 22(c)] occurs coupling with the MIT.

Table 12. Magnetic moment values for each Co site with magnetic structure in Fig. 14(d). R_{wp} = 10.2 %.

Phase FM	Co1	Co2
M(μ_B) at 80K	1.05(7)	-0.90(7)

4.2.4. Mechanism for MIT induced by hole doping

The evidence of hole doping SST were also found by the Curie-Weiss fitting on inverse susceptibility curve [Fig. 23 (a)] the in the range of 200 – 400 K, which gives 3.74 μ_B average average magnetic effective moment for $PrBaCo_2O_{5.74}$. Comparing with the 2.50 μ_B of $PrBaCo_2O_{5.52}$, we believe that the spin state of some Co^{3+} ions changes during the hole doping induced MIT, because only 25% Co^{4+} (S= ½, μ_{eff} = 1.73 μ_B) cannot make the difference of 1.24 μ_B. Actually, the hole doping SST was also observed in the well known $LaCoO_3$ system, where the ground state is composed of LS Co^{3+} ions, and a small amount of hole doping, e.g., $La_{1-x}Sr_xCoO_3$, x=0.001, give rise to a SST to IS. [55,56] By measurements of the magnetization and fitting with the modified Brillouin function, it was demonstrated that a doped single hole shows an extremely high spin number, S=10 –16, which means that a hole with O 2p-state character causes a local spin-state transition (low-spin to intermediate-spin) over 10 –16 Co sites around itself, perhaps due to strong $2p\sigma$ -$3de_g$ hybridization. [57]

Since MITs induced by temperature and hole doping are accompanied by the same structure phase transition and SST, it is highly possible that they also share the same scenario. Moreover, the O-K XAS spectra of $PrBaCo_2O_{5+x}$ [Fig. 23 (b)] present similar behavior as those of $PrBaCo_2O_{5.2}$ [Fig. 14 (b)], the spectrum in the metal phase ($PrBaCo_2O_{5.62}$) shifts to a lower energy side, indicating the decrease of the band gap. Taking into account all these results, we propose the same mechanism for both temperature and hole doping induced MITs.

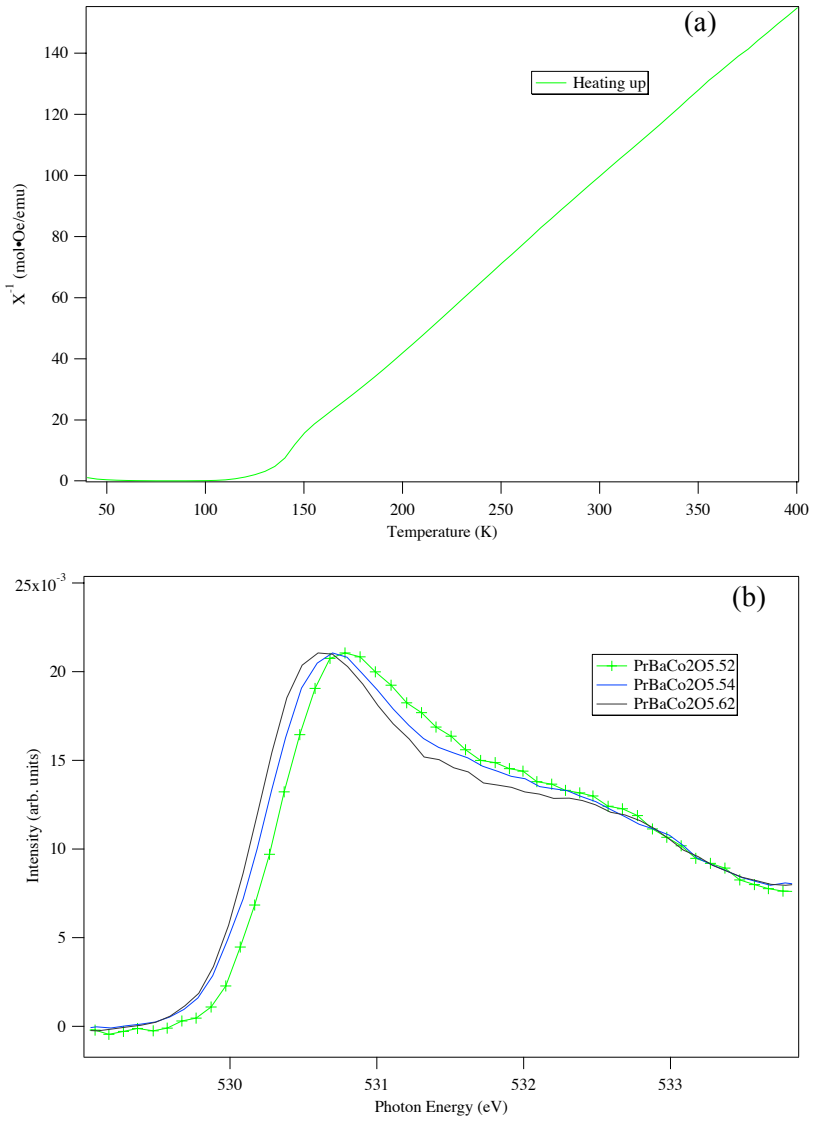

Fig. 23 (a) Inverse susceptibility 1/X of $PrBaCo_2O_{5.74}$ measured under a field of 100 Oe after cooling dowen to 40 K in the zero field (ZFC). (b) O-K XAS spectra of $PrBaCo_2O_{5+x}$ (x = 0.52, 0.54 and 0.62) at room temperature.

Chapter 5 Conclusion

Through the systematic study on the $PrBaCo_2O_{5.5+\delta}$, we could draw a phase diagram as shown in Fig. 24, which is divided into two phases, insulator and metal. In insulator phase, the crystal structure is Pmma ($2a_p \times 2a_p \times 2a_p$) and LS Co^{3+} ions occupy partially in the octahedral site. When entering to the metal phase, a SST to IS or HS occurs coupling with the structure phase transition to Pmmm ($a_p \times 2a_p \times 2a_p$) where the super lattice along a axis vanishes.

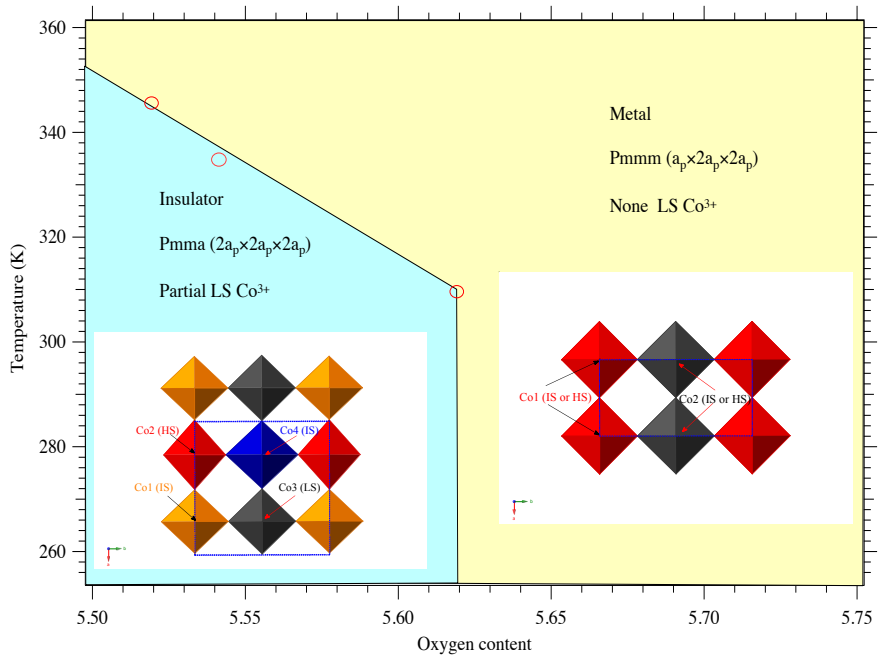

Fig. 24 Phase diagram of $PrBaCo_2O_{5+x}$. The red open circles are MIT temperatures determined from the resistivity measurement. Blue region is the insulator phase, and yellow region metal phase. The drawing of polyhedrons in blue region indicates the Pmma ($2a_p \times 2a_p \times 2a_p$) structure (ab plan view) with the spin state assigned in each Co site, while that in the yellow region indicates the Pmmm ($a_p \times 2a_p \times 2a_p$) structure (ab plan view) with the spin state assigned in each Co site.

** The terminology of "insulator" and "metal" here is just to distinguish the large difference in resistivity, because even in the "metal" phase, it behaves like a semiconductor of which the resistivity is in negative correlation with temperature.*

The MITs induced by temperature and hole doping in $PrBaCo_2O_{5.5+\delta}$ share a common mechanism. As pointed above, the "spin blockade" model proposed in Ref. [20,36] fails to simultaneously explain the MITs induced by both temperature and hole doping. We here

propose a new mechanism, that is half of the IS octahedral Co^{3+} ions in metal phase switch into the LS state, and the resultant empty e_g orbital significantly decreases the hopping parameter, making the insulator phase.

It is noted that the direct observation of LS Co^{3+} ions in $PrBaCo_2O_{5.5}$ by magnetic structure analysis is very essential to clarify the mechaism for MITs in this system. Also the work in hole doping induced MIT, which was not paid much attention before, help us to complete the phase diagram. To the best of our knowledge, it is the first time to report the hole doping induced SST in this system.

We expect the MITs for $RBaCo_2O_{5.5+\delta}$ (R: from Nd to Dy) will have the same scenario as $PrBaCo_2O_{5+x}$ on the basis of the identical structure phase transition. As for $RBaCo_2O_{5.5+\delta}$ (R: Ho and Y), the behaviors of structure and properties are different from those of $RBaCo_2O_{5.5+\delta}$ (R: from Pr to Dy). So at this moment, it is hard to say whether they share the same mechanism or not. So systematic studies on $RBaCo_2O_{5.5+\delta}$ with light to heavy rare earth elements are indispensable.

Acknowledgement

The author is grateful for Prof. Takashi Kamiyama of The Graduate University for Advanced Studies (Japan) and High Energy Accelerator Research Organization (Japan) for the supervision and orientation throughout this research. The author also appreciate Dr. Shuki Torii, Dr. Masao Yonemura, Dr. Yoshihisa Ishikawa, and Dr. Sanghyun Lee of High Energy Accelerator Research Organization (Japan) for the help of neutron experiment, Prof. Kanta Ono, Dr. Nobuhito Inami and Dr. Tetsuro Ueno of High Energy Accelerator Research Organization (Japan) for the help of DSD and XAS experiment, Prof. Yingxia Wang, Ms. Xiaohuan Lin of Peking University (China) for the help of sample synthesis, XRD and XPS experiment, Prof Masatoshi Sato, Dr. Taketo Moyoshi of Comprehensive Research Organization (Japan) for Science and Society for the help of magnetization and resistivity measurements. The author thanks Prof. Yukio Noda of Tohoku University (Japan), Dr. Junrong Zhang of Institute of High Energy Physics (China) and Dr. Fangwei Wang of Institute of Physics (China) for all the helpful discussions.

Reference

[1] C. Martin, a. Maignan, D. Pelloquin, N. Nguyen, and B. Raveau, Appl. Phys. Lett. **71**, 1421 (1997).

[2] I. . Troyanchuk, N. . Kasper, D. . Khalyavin, H. Szymczak, R. Szymczak, and M. Baran, Phys. Rev. Lett. **80**, 13 (1998).

[3] A. Maignan, C. Martin, D. Pelloquin, N. Nguyen, and B. Raveau, J. Solid State Chem. **142**, 247 (1999).

[4] D. Akahoshi and Y. Ueda, J. Phys. Soc. Japan **68**, 736 (1999).

[5] D. Akahoshi and Y. Ueda, J. Solid State Chem. **156**, 355 (2001).

[6] Y. Moritomo, T. Akimoto, M. Takeo, A. Machida, E. Nishibori, M. Takata, M. Sakata, K. Ohoyama, and A. Nakamura, Phys. Rev. B **61**, 325 (2000).

[7] H. Kusuya, A. Machida, Y. Moritomo, K. K. Kato, E. Nishibori, M. Takata, M. Sakata, and A. Nakamura, **70**, 3577 (2001).

[8] M. Respaud, C. Frontera, J. García-Muñoz, M. Aranda, B. Raquet, J. Broto, H. Rakoto, M. Goiran, A. Llobet, and J. Rodríguez-Carvajal, Phys. Rev. B **64**, 214401 (2001).

[9] C. Frontera, J. García-Muñoz, A. Llobet, and M. Aranda, Phys. Rev. B **65**, 180405 (2002).

[10] N. Mott, Rev. Mod. Phys. **40**, 677 (1968).

[11] M. Imada, A. Fujimori, and Y. Tokura, Rev. Mod. Phys. **70**, 1039 (1998).

[12] N. Mott and R. Peierls, Proc. Phys. Soc. **49**, 72 (1937).

[13] N. Mott, Proc. Phys. Soc. **62**, 416 (n.d.).

[14] J. Hubbard, Proc. R. Soc. A Math. Phys. Eng. Sci. **276**, 238 (1963).

[15] J. Hubbard, Proc. R. Soc. A Math. Phys. Eng. Sci. **277**, 237 (1964).

[16] J. Hubbard, Proc. R. Soc. A Math. Phys. Eng. Sci. **281**, 401 (1964).

[17] C. Zener, Phys. Rev. **82**, 403 (1950).

[18] J. Zaanen, A. Sawatzky, and J. W. Allen, Phys. Rev. Lett. **55**, 418 (1985).

[19] A. Taskin, A. Lavrov, and Y. Ando, Phys. Rev. B **71**, 134414 (2005).

[20] A. Taskin and Y. Ando, Phys. Rev. Lett. **95**, 176603 (2005).

[21] D. Chernyshov, G. Rozenberg, E. Greenberg, E. Pomyakushina, and V. Dmitriev, Phys. Rev. Lett. **103**, 125501 (2009).

[22] A. Taskin, A. Lavrov, and Y. Ando, Phys. Rev. Lett. **90**, 227201 (2003).

[23] M. Soda, Y. Yasui, Y. Kobayashi, T. Fujita, M. Sato, and K. Kakurai, J. Phys. Soc. Japan **75**, 104708 (2006).

[24] L. Malavasi, M. Brunelli, Y. Diaz-Fernandez, B. Pahari, and P. Mustarelli, Phys. Rev. B **80**, 153102 (2009).

[25] F. Fauth, E. Suard, V. Caignaert, and I. Mirebeau, Phys. Rev. B **66**, 184421 (2002).

[26] V. Plakhty, Y. Chernenkov, S. Barilo, A. Podlesnyak, E. Pomjakushina, E. Moskvin, and S. Gavrilov, Phys. Rev. B **71**, 214407 (2005).

[27] H. Luetkens, M. Stingaciu, Y. Pashkevich, K. Conder, E. Pomjakushina, A. Gusev, K. Lamonova, P. Lemmens, and H. Klauss, Phys. Rev. Lett. **101**, 017601 (2008).

[28] D. Khalyavin, D. Argyriou, U. Amann, A. Yaremchenko, and V. Kharton, Phys. Rev. B **75**, 134407 (2007).

[29] F. Fauth, E. Suard, V. Caignaert, and B. Domeng, **174**, 163 (2001).

[30] M. Soda, Y. Yasui, T. Fujita, T. Miyashita, M. Sato, and K. Kakurai, J. Phys. Soc. Japan **72**, 1729 (2003).

[31] Y. Chernenkov, V. Plakhty, V. Fedorov, S. Barilo, S. Shiryaev, and G. Bychkov, Phys. Rev. B **71**, 184105 (2005).

[32] Y. Chernenkov, V. Plakhty, A. Gukasov, S. Barilo, S. Shiryaev, G. Bychkov, V. Hinkov, V. Fedorov, and V. Chekanov, Phys. Lett. A **365**, 166 (2007).

[33] D. Chernyshov, V. Dmitriev, E. Pomjakushina, K. Conder, M. Stingaciu, V. Pomjakushin, A. Podlesnyak, A. Taskin, and Y. Ando, Phys. Rev. B **78**, 024105 (2008).

[34] J. Padilla-Pantoja, C. Frontera, O. Castaño, and J. L. García-Muñoz, Phys. Rev. B **81**, 132405 (2010).

[35] J. Padilla-Pantoja, C. Frontera, J. Herrero-Martín, and J. García-Muñoz, J. Appl. Phys. **111**, 07D710 (2012).

[36] A. Maignan, V. Caignaert, B. Raveau, D. Khomskii, and G. Sawatzky, Phys. Rev. Lett. **93**, 026401 (2004).

[37] C. Frontera, J. García-Muñoz, A. Carrillo, C. Ritter, D. Martín y Marero, and A. Caneiro, Phys. Rev. B **70**, 184428 (2004).

[38] C. Frontera, J. García-Muñoz, A. Carrillo, A. Caneiro, C. Ritter, and D. Martín y Marero, J. Appl. Phys. **97**, 10C106 (2005).

[39] S. Streule, a Podlesnyak, J. Mesot, M. Medarde, K. Conder, E. Pomjakushina, E. Mitberg, and V. Kozhevnikov, J. Phys. Condens. Matter **17**, 3317 (2005).

[40] C. Frontera, A. Caneiro, A. E. Carrillo, and J. Oro, Chem. Mater. **17**, 5439 (2005).

[41] G. Kim, S. Wang, A. Jacobson, L. Reimus, P. Brodersen, and C. Mims, J. Mater. Chem. **17**, 2500 (2007).

[42] K. Zhang, L. Ge, R. Ran, Z. Shao, and S. Liu, Acta Mater. **56**, 4876 (2008).

[43] R. Oishi-Tomiyasu, J. Appl. Crystallogr. **46**, 1277 (2013).

[44] R. Oishi-Tomiyasu, M. Yonemura, T. Morishima, a. Hoshikawa, S. Torii, T. Ishigaki, and T. Kamiyama, J. Appl. Crystallogr. **45**, 299 (2012).

[45] R. Oishi, M. Yonemura, Y. Nishimaki, S. Torii, a. Hoshikawa, T. Ishigaki, T. Morishima, K. Mori, and T. Kamiyama, Nucl. Instruments Methods Phys. Res. Sect. A Accel. Spectrometers, Detect. Assoc. Equip. **600**, 94 (2009).

[46] J. Rodriguez-carvajal, Phys. B **192**, 55 (1993).

[47] A. S. Wills, Phys. B **278**, 680 (2000).

[48] A. Kotani and Y. Toyozawa, J. Phys. Soc. Japan **37**, 912 (1974).

[49] M. Oku and K. Hirokawa, J. Electron Spectros. Relat. Phenomena **8**, 475 (1976).

[50] Z. Hu, H. Wu, T. C. Koethe, S. N. Barilo, S. V Shiryaev, G. L. Bychkov, C. Schüßler-Langeheine, T. Lorenz, a Tanaka, H. H. Hsieh, H.-J. Lin, C. T. Chen, N. B. Brookes, S. Agrestini, Y.-Y. Chin, M. Rotter, and L. H. Tjeng, New J. Phys. **14**, 123025 (2012).

[51] M. B. Maple, N. P. Butch, N. A. Frederick, P.-C. Ho, J. R. Jeffries, T. A. Sayles, T. Yanagiswa, W. M. Yuhasz, S. Chi, H. J. Kang, J. W. Lynn, P. Dai, S. K. McCall, M. W. McElfresh, M. J. Fluss, Z. Henkie, and A. Pietraszko, PNAS **103**, 6783 (2006).

[52] W.-H. Li, K. J. Chang, W. T. Hsieh, and L. K. C, Phys. Rev. B **48**, (1993).

[53] Z. Hu, H. Wu, M. Haverkort, H. Hsieh, H. Lin, T. Lorenz, J. Baier, a. Reichl, I. Bonn, C. Felser, a. Tanaka, C. Chen, and L. Tjeng, Phys. Rev. Lett. **92**, 207402 (2004).

[54] C. Chang, Z. Hu, H. Wu, T. Burnus, N. Hollmann, M. Benomar, T. Lorenz, a. Tanaka, H.-J. Lin, H. Hsieh, C. Chen, and L. Tjeng, Phys. Rev. Lett. **102**, 116401 (2009).

[55] Y. Tokura, Y. Okimoto, S. Yamaguchi, H. Taniguchi, T. Kimura, and H. Takagi, **58**, 1699 (1998).

[56] Y. Onose and Y. Tokura, Phys. Rev. B **73**, 174421 (2006).

[57] S. Yamaguchi, Y. Okimoto, H. Taniguchi, and Y. Tokura, Phys. Rev. B **53**, R2926 (1996).